Engineering Structures 195 (2019) 22–50

Contents lists available at ScienceDirect

Engineering Structures

journal homepage: www.elsevier.com/locate/engstruct

Efficient modeling of flexural and shear behaviors in reinforced concrete beams and columns subjected to low-velocity impact loading

Wei Fan[a,*], Bin Liu[a,b], Xu Huang[c], Yang Sun[a]

[a] Key Laboratory for Wind and Bridge Engineering of Hunan Province, College of Civil Engineering, Hunan University, Changsha 410082, China
[b] Hualan Design & Consulting Group, Nanning 530011, China
[c] Department of Civil Engineering, University of Toronto, ON M5S 1A4, Canada

ARTICLE INFO

Keywords:
Efficient modeling
Reinforced concrete beams and columns
Impact responses
Fiber-section beam-column elements
Shear behaviors

ABSTRACT

Detailed finite element (FE) models with 3-D solid elements are typically used to simulate impact behaviors of reinforced concrete (RC) beams and columns. However, the method usually requires a substantial amount of time and effort to model concrete and reinforcement and conduct nonlinear contact-impact analyses. Also, the accuracy of the method cannot be guaranteed due to the limitations in concrete material models implemented in general-purpose FE codes. In this paper, an efficient modeling method is proposed to capture both flexural and shear behaviors of RC beams and columns under low-velocity impact loading. A macroelement-based contact model was developed in the proposed method to capture interaction behaviors between impacting objects and RC members. In the contact model, a compression-only spring with an initial gap behavior was used to account for the stiffness and the kinematic response of an impacting object, and a combination of an elastic spring and a viscous damper in parallel was employed to simulate the contact stiffness and damping. By properly approximating the strain-rate effects, traditional fiber-section elements were demonstrated to be capable of predicting impact-induced flexural failures for RC members. On this basis, a general approach for both flexural- and shear-critical RC columns under impact loading was presented with the inclusion of additional shear springs in the fiber-section elements. Nearly fifty impact tests on RC beams and columns reported in the literature were employed to validate the proposed modeling method. Comparisons between the experimental and numerical results indicate that failure modes of the impacted members can be identified explicitly by the use of the proposed modeling method. Also, reasonable agreements were achieved for the impact forces and the impact-induced responses obtained from the impact tests and the analyses. The proposed method can be readily implemented without coding in any FE software as long as traditional fiber-section elements, and discrete macroelements are available. This feature would offer an advantage for the applications of the proposed method such as when assessing the structural response and vulnerability of a bridge structure subjected to vessel and vehicle collisions.

1. Introduction

Numerous catastrophic accidents such as vessel or vehicle collisions with reinforced concrete (RC) columns happened in recent years around the world [1–4]. In this context, many impact tests have been carried out to clarify the behaviors of RC beams and columns subjected to impact loading (e.g. [5–11]). However, it might be unrealistic always to perform physical experiments because of the massive investments in the economy and time. On the other hand, relatively small-scale RC specimens are usually used in these impact tests due to the limits in laboratory space and the capacity of impact testing facilities. Strictly speaking, these experimental results only partially addressed the impact behaviors of full-scale RC members. Hence, analysis methods should be well established based on these test data to efficiently and accurately assess the responses of RC members under impact loading.

Currently, many studies have been carried out to develop detailed FE models with the use of general-purpose contact-impact nonlinear FE codes (e.g., LS-DYNA and ABAQUS) for RC members under impact loads [12–17]. Among these studies, 3-D solid elements were mostly used for concrete while beam/truss elements were employed to model reinforcing rebars. However, the use of such methods requires extensive efforts for creating models of impacting objects (e.g., vessel or vehicle) and impacted RC structures (e.g., bridge pier and pile) [18–20]. In addition, running nonlinear contact-impact analysis using general-purpose FE programs is computationally expensive such that high-performance computing techniques, i.e., supercomputers, have been

* Corresponding author.
E-mail address: wfan@hnu.edu.cn (W. Fan).

https://doi.org/10.1016/j.engstruct.2019.05.082
Received 3 January 2019; Received in revised form 25 May 2019; Accepted 26 May 2019
Available online 04 June 2019

used in some of the recent studies [18–20]. Also, since there are still some limitations for concrete material models implemented in general-purpose FE programs, the reliability of analysis results cannot always be guaranteed [7,21]. It could be a tricky task when using this method to capture shear behaviors in RC beams and columns under impact loading. A widely-accepted FE method for shear-critical RC members subjected to impact loading is still lacking [22].

In addition to the detailed FE modeling methods, some simplified methods have been developed to evaluate the impact responses of RC members [6,16,23,24]. These methods are characterized by the simplification of the impacted RC structures as mass-spring systems with a single or two degree-of-freedom (DOF), which significantly increases the computational efficiency. However, most of them only demonstrated the satisfactory performance on predicting the impact-induced responses for flexural-critical RC members and few attempts have been made to accurately capture the behaviors of shear-critical RC members [6,16]. Zhao et al. [23] recently extended the two-DOF models to three-DOF models to predict both overall flexural responses and shear plug failure around drop hammers of RC beams due to drop-hammer impacts. Although the simplified methods improve the computational efficiency, they are restained by the difficulties in simplifying the impacted structures (e.g., bridges) into single or two DOF systems in real-world impact problems such as vessel or vehicle collisions with bridge structures.

Due to the above limitations in efficiency and applicability, it is necessary to develop an alternative modeling approach for efficient and accurate assessment of RC structures under impact loads. For example, Guner and Vecchio [22] developed a simplified model based on nonlinear beam-column elements to simulate behaviors of RC beams under drop-hammer impacts and implemented its formulation into the computer code VecTor5. However, the method is only applicable for planar frames and thus cannot be applied to three-dimensional impact problems, such as oblique collision events or cases where both superstructure and bridge piers need to be explicitly modeled [25,26]. Therefore, further efforts need to be made to develop a simple and efficient modeling method that would be widely applicable for impact simulations of RC structures.

In the above context, a new modeling method was proposed in this paper to efficiently analyze both flexural and shear failures of RC beams and columns subjected to low-velocity impact loading. Nearly fifty drop-hammer impact tests on RC members were collected in this study to validate the proposed method. Specifically, a macroelement-based model was developed to model the local interaction behavior between drop hammers and the RC members. For RC beams and columns with flexure-dominated failures, common fiber-based beam-column elements were demonstrated to be capable of yielding reliable results after approximately accounting for strain-rate effects. Subsequently, a general modeling method of RC beams and columns was presented to analyze both flexural and shear responses to impact loads. Obvious advantages such as high efficiency and low requirements in elements would significantly facilitate the application of the proposed modeling method into real-world problems (e.g., vessel/vehicle-bridge collision analysis).

2. Modeling of flexure-dominated failure in RC beams

The proposed modeling method is first presented to capture the impact behaviors of RC beams with flexure-dominated failure modes. Fig. 1 illustrates the proposed model for impact simulations of flexure-critical RC beams. This model consists of an impacting object (e.g., drop hammer), an impacted RC member and a macroelement-based system to simulate the local interaction between the impacting objects and the RC members. Detailed modelings of these three components are presented in the following sections.

2.1. Modeling of impacting object and initial impact velocity

The impacting object can be an errant vessel, a vehicle or any other object in practical impact problems. For vessel-bridge collisions, Consolazio and Cowan [18] and Fan et al. [19] have developed some simplified mass-spring-dashpot systems to represent the mechanical behavior of a barge or ship. They were demonstrated to be useful and efficient in vessel-bridge collision analysis [18,19]. How to model different types of impacting objects is beyond the scope of this paper. For validation, drop-hammer impact tests on beams were mainly discussed and simulated in this study. Hence, the rigid drop hammer was regarded as the impacting object and modeled as a simplified mass-spring system. As shown in Fig. 1, a lumped mass element A and an elastic spring element were used to model the mass (M_h) and stiffness (K_h) of a drop hammer, respectively.

The elastic spring element is only compressible to simulate the separation between the impacting object and the impacted structure after collisions. It is easy to apply an initial impact velocity to a lumped mass when the solution methodology of FE code (e.g., LS-DYNA) is based on explicit time integration. Usually, initial impact speeds cannot be given directly in the FE code with an implicit solver (e.g., OpenSees and Sap2000). In this case, the initial impact speed (V_0) can be obtained by exerting an instant load (or impulse $I = Pt$) on the lumped mass as follows:

$$V_0 = Pt/M_h \tag{1}$$

where P is the impulsive force for obtaining the initial impact speed (V_0); t is the time duration of the impulsive force. In addition, an initial gap should be added in the compression-only spring of the drop hammer to ensure that the contact between the drop hammer and the impacted member is triggered after the lumped mass reaches the expected initial impact speed. Accordingly, the initial gap (GA) should meet the following requirement:

$$\mathrm{GA} \geqslant V_0 t/2 \tag{2}$$

In this study, the above modeling strategies are achieved through the use of the open-source analysis platform OpenSees [27]. Specifically, the compression-only spring with an initial gap is defined using the uniaxial material *ElasticPPGap*, and the corresponding force-displacement relationship is shown in Fig. 2(a). Since the drop hammer is typically more rigid than the impacted member, K_h was set to be a relatively high value of 1×10^9 N/m in this paper.

2.2. Modeling interaction using macroelements

Similar to the analytical model developed by Fujikake et al. [6], a macroelement-based model including an elastic spring and a viscous damper in parallel was employed to simulate the contact stiffness (K_c) and damping (D_a) between the drop hammer and the impacted structure, as shown in Fig. 1(c). In OpenSees, the uniaxial materials *contact-spring* (Fig. 2(b)) and *linear-viscous-damper* (Fig. 2(c)) can be used to consider the contact stiffness and damping, respectively. The approximate methods provided in [6,28] were adopted to determine the values of the contact stiffness and damping. The contact stiffness usually has a significant influence on the peak impact force but does not markedly affect the displacement of the impacted RC member [6,28].

2.3. Modeling of RC members

Nonlinear beam-column elements with fiber-based discretizations in the members' cross sections were used to model RC members under lateral impact loading, as shown in Fig. 1(d). In the OpenSees, two different types of nonlinear beam-column elements are available, i.e., force-based elements and displacement-based elements. Distinct from the displacement-based elements, the force-based elements allow a physically meaningful plastic hinge length to be specified for large

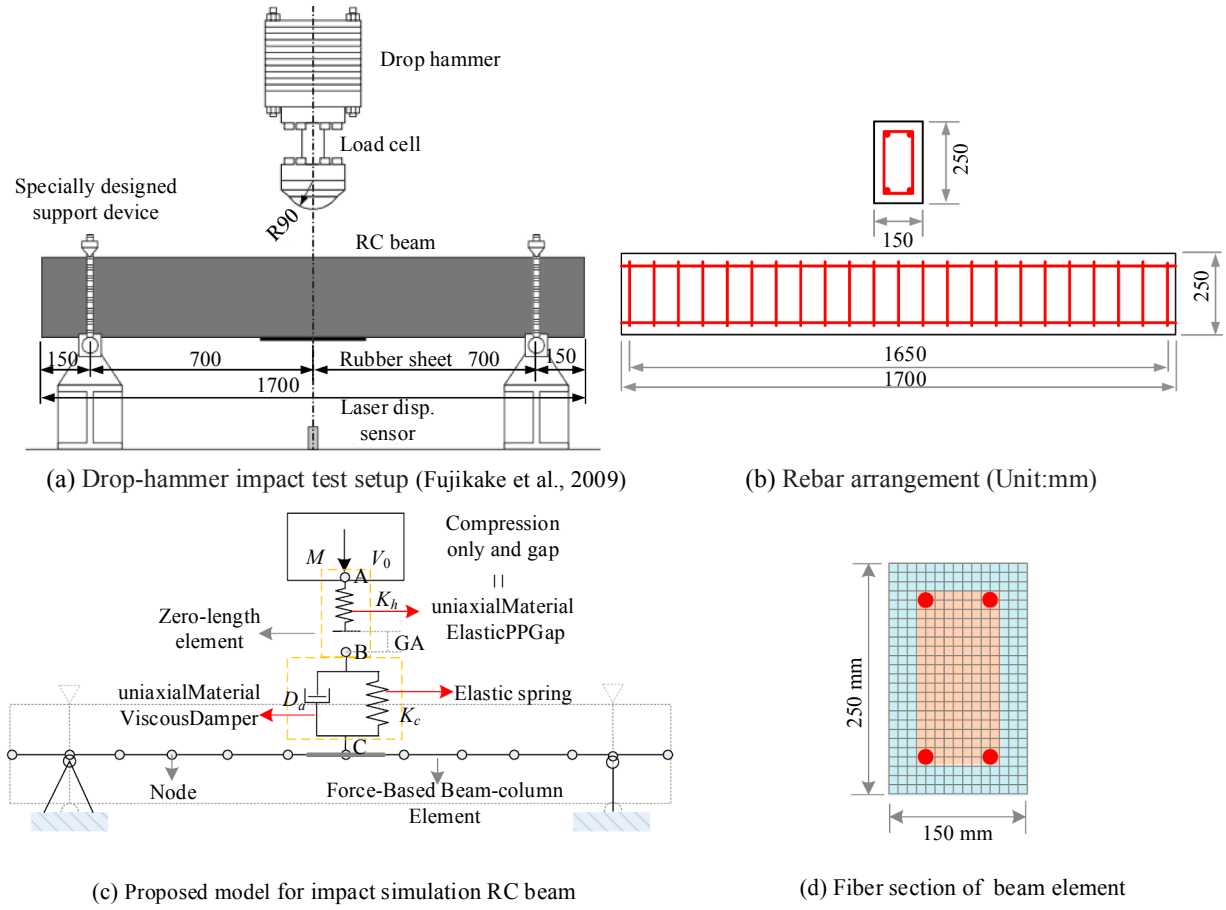

(a) Drop-hammer impact test setup (Fujikake et al., 2009)

(b) Rebar arrangement (Unit:mm)

(c) Proposed model for impact simulation RC beam

(d) Fiber section of beam element

Fig. 1. Proposed model to predict flexural responses of RC beams under impact loading.

deformations at the small portion (e.g., contact-impact zone). Past impact tests on reinforced concrete members [6,7] indicate that a visible plastic hinge usually occurs around the contact-impact region. Thus, nonlinear force-based elements with multiple integration points were employed in this study to simulate reinforced concrete members. A plastic hinge with the length equal to the height of the member's cross-section [29] was specified at the contact-impact zone (see Fig. 1). It is worth mentioning that the deformation capacity of the impacted members would be significantly underestimated for the absence of the plastic hinge in the contact-impact point because deformations are too concentrated at the impact point (e.g., point C in Fig. 1) that connects to discrete contact macroelements. Hence, the above treatment is also of great importance in the modeling of reinforced concrete members subjected to impact loading.

The typical fiber section in the OpenSees [27] was used to the cross section of nonlinear beam-column elements. As shown in Fig. 1(d), fiber-based cross sections were composed of cover concrete fibers, core concrete fibers and reinforcing steel fibers. Concrete was modeled by a uniaxial Propovics concrete material model with degraded linear unloading/reloading stiffness in accordance with the work of Karsan-Jirsa [30] and tensile strength with an exponential decay (i.e., Concrete04 material in OpenSees [27]). Cover concrete in compression was defined using the model proposed by Popovics [31]. For core concrete, FE simulations using the above fiber-based beam-column elements were

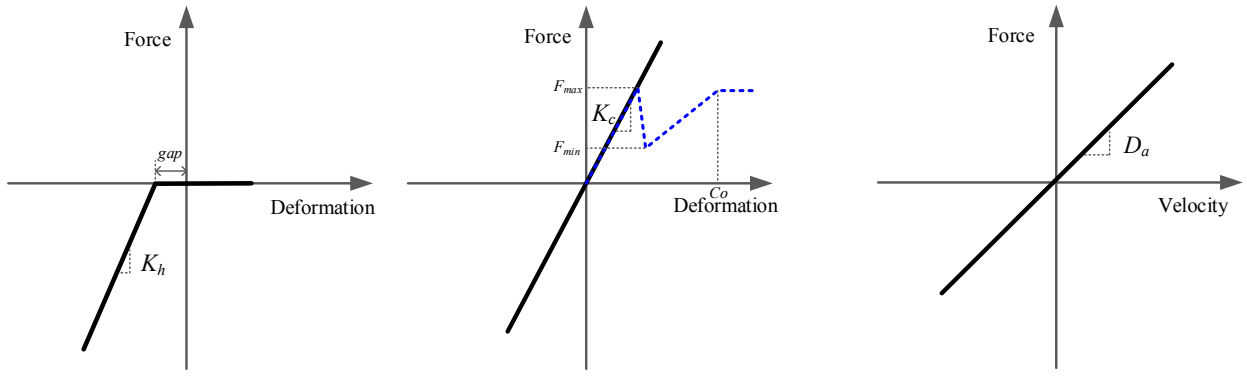

(a) Compression-only spring with a gap

(b) Uniaxial material for contact stiffness

(c) Linear viscous material for contact damping

Fig. 2. Constitutive relations of discrete elements regarding impacting object and contact-impact model.

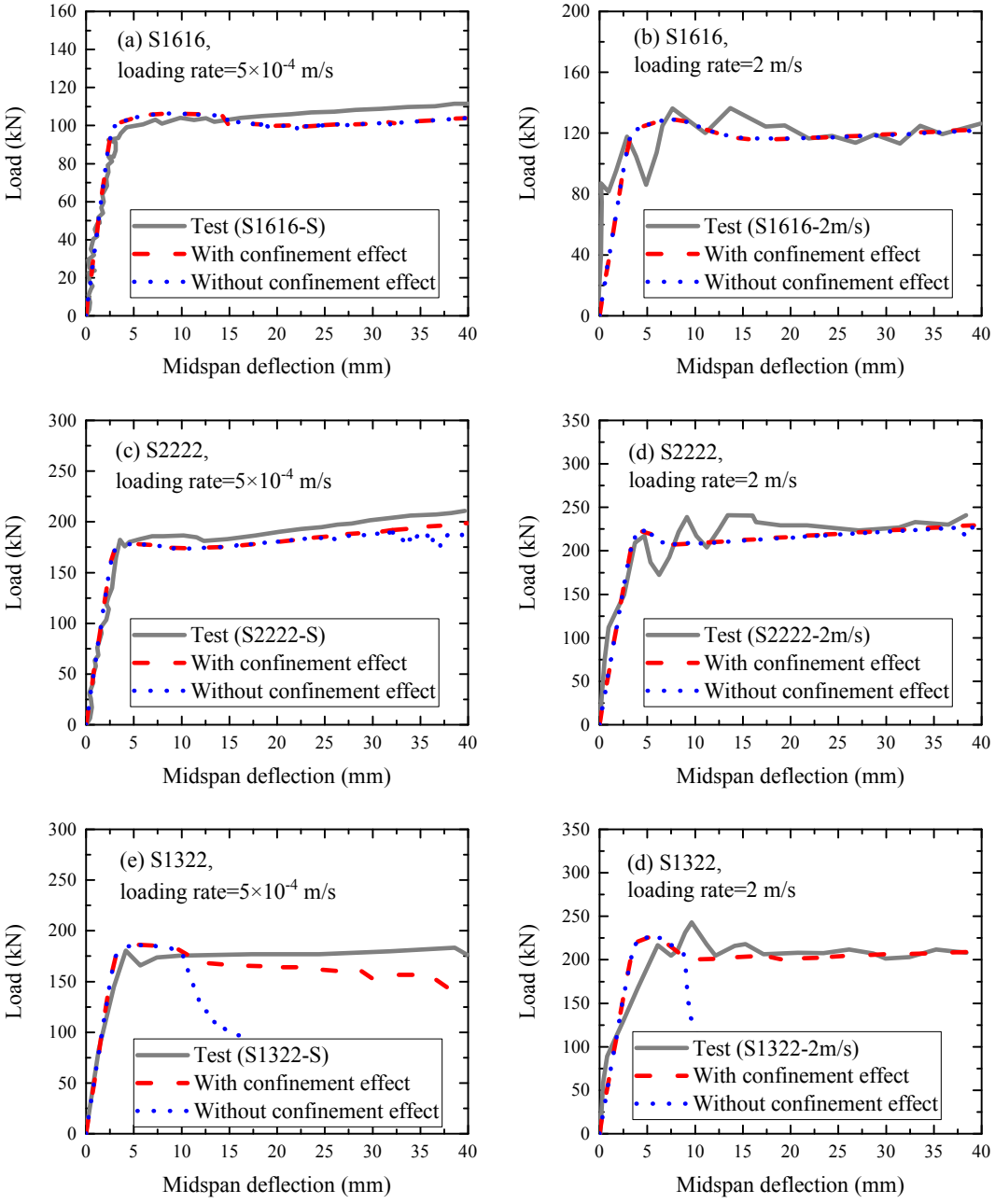

Fig. 3. Comparisons of load-midspan deflection relations between experimental and numerical results.

performed to examine the influence of confinement effect. The flexural loading tests performed by Fujikake et al. [6] were simulated, which had the same RC beams S1616, S1322, and S2222 as the subsequent impact loading tests. As shown in Fig. 3, good agreements were observed between the experimental data and the FE results for specimens S1616 and S2222 no matter whether the confinement effect was considered or not. However, the confinement effect was significant for specimen S1322. The FE results of specimen S1322 were in good agreement with the experimental data when including the confinement effect. In contrast, the numerically-obtained ductility was much lower than that measured from the experiment. The discrepancies between specimens S1322 and S2222 (or S1616) may be attributed to the differences in reinforcement arrangements in the compression side of the beams. Specimens S1616 and S2222 had relatively high longitudinal reinforcement ratios in the compression side so that the failure did not appear too early in the compression side. The core concrete in the compression side was under bi-direction compression due to the presence of transverse bars. For specimen S1322, the longitudinal reinforcement ratio was low, and the contribution of the core concrete in the compression side to the ductility became significant. In this case, omitting the confinement effect would significantly underestimate the ductility of a beam. Besides, including the confinement effect had no negative impacts on the responses of specimens S2222 and S1616. Ou and Nguyen [29] pointed out that the confinement effect should be included for the analyses of RC beams. Therefore, the core concrete was modeled by the confined concrete model in this study.

The uniaxial Giuffre-Menegotto-Pinto model (*Steel02* Material in OpenSees) was used to simulate reinforcing steel. Material properties used in the analyses are consistent with the experimental data for the impacts tests on RC beams conducted by Fujikake et al. [6]. Different from the static or seismic analyses, strain-rate effects regarding concrete and steel materials need to be taken into account in impact simulations. For concrete in compression, the formulas developed by Fujikake et al. [6] can be used to estimate the dynamic increase factor

(DIF_c) as follows:

$$DIF_c = \frac{f'_{cd}}{f'_c} = \left(\frac{\dot{\varepsilon}}{\dot{\varepsilon}_{sc}}\right)^{0.006[\log \dot{\varepsilon}/\dot{\varepsilon}_{sc}]^{1.05}} \quad \text{for } \dot{\varepsilon} \geqslant \dot{\varepsilon}_{sc} \tag{3}$$

where $\dot{\varepsilon}$ is the strain-rate of concrete; $\dot{\varepsilon}_{sc}$=1.2 × 10^{-5}; f'_{cd} is the dynamic uniaxial compressive strength; f'_c is the static uniaxial compressive strength. Theoretically, the strain-rate effect of concrete in tension can be included as well. However, numerical results indicate that the influence of the strain-rate effect of concrete in tension is not pronounced when using nonlinear fiber-based beam-column elements in impact simulations. Also, including the strain-rate effect of concrete in tension might lead to convergence issues. For these reasons, the strain-rate effect of concrete in tension was omitted in this study. Similar to [6,32], the strain-rate effect of reinforcing steel was considered by the equation provided by the Japan Society of Civil Engineers (JSCE) [33] as follows:

$$DIF_s = \frac{f_{syd}}{f_{sys}} = 1.202 + 0.040 \times \log_{10} \dot{\varepsilon} \geqslant 1.0 \tag{4}$$

where DIF_s is the dynamic increase factor of reinforcing steel due to the strain-rate effect; f_{syd} and f_{sys} are the static and dynamic yield strengths of reinforcing steel, respectively.

The direct use of these equations to consider the strain rate effects in existing FE codes not only requires access to the source code but also involves cumbersome modifications of the code, which sharply limits the application of the proposed method. Hence, a simple treatment was employed in this paper to approximate the strain-rate effects on impact-induced responses.

In the elastic regime, the curvature ϕ_E and the curvature rate $\dot{\phi}_E = d\phi_E/dt$ at a given section can be determined from linear elastic theory for a flexural member as follows:

$$\phi_E = \frac{M}{EI} = C_L u \text{ for } 0 \leqslant u \leqslant u_y \tag{5}$$

$$\dot{\phi}_E = \frac{d\phi_E}{dt} = C_L \dot{u} \text{ for } 0 \leqslant u \leqslant u_y \tag{6}$$

where M is the moment for a given cross-section; E and I are the elastic modulus and moment of inertia of beams, respectively; u and $\dot{u}$ are the displacement and velocity for a given location, respectively; u_y is the yield displacement; C_L is the coefficient related to load characteristics. For a concentrated load, $C_L = 12/l^2$ at the mid-span section in the elastic regime (where l is the span length of the beam).

In the plastic regime, a concentrated plastic hinge is typically formed at the cross-section corresponding to the contact-impact load point. As shown in Fig. 4, the curvature ϕ_p and the curvature rate $\dot{\phi}_p$ in the plastic regime can be determined by

$$\begin{aligned}\phi_p &= \phi_y + \frac{\theta_p}{l_p} = \phi_y + \left(\frac{u_p}{l_x} + \frac{u_p}{l - l_x}\right)\frac{1}{l_p} \\ &= \phi_y + \left(\frac{1}{l_x} + \frac{1}{l - l_x}\right)\frac{u - u_y}{l_p} \text{ for } u \geqslant u_y\end{aligned} \tag{7}$$

$$\dot{\phi}_p = \frac{d\phi_p}{dt} = C_L \dot{u} = \left(\frac{1}{l_x} + \frac{1}{l - l_x}\right)\frac{\dot{u}}{l_p} \text{ for } u \geqslant u_y \tag{8}$$

where θ_p is the plastic rotation; l_p is the length of the plastic hinge; ϕ_y is the curvature corresponding to the yield; u_p is the plastic displacement; l_x is the distance from the force-applied location to one end of the beam, as illustrated in Fig. 4. $C_L = 4/(ll_p)$ when the impact load is applied at the mid-span of the impacted beam [34]. Considering the fact that RC concrete members under impact loading are mainly governed by their nonlinear behaviors and the impact-induced displacements tend to significantly exceed the elastic displacement limit, the coefficient (e.g., $C_L = 4/(ll_p)$) in the plastic regime is assumed for the entire impact process.

Like [34], the strain rates of concrete and reinforcing steel can be calculated for a given cross-section through the following equations:

$$\dot{\varepsilon}_{ec} = \dot{\phi}_p \cdot \bar{x} = C_L \cdot \dot{u} \cdot \bar{x} \tag{9}$$

$$\dot{\varepsilon}_{est} = \dot{\phi}_p \cdot (d - \bar{x}) = C_L \cdot \dot{u} \cdot (d - \bar{x}) \tag{10}$$

$$\dot{\varepsilon}_{esc} = \dot{\phi}_p \cdot (\bar{x} - d') = C_L \cdot \dot{u} \cdot (\bar{x} - d') \tag{11}$$

where $\dot{\varepsilon}_{ec}$ is the strain rate of concrete at a given cross-section; $\dot{\varepsilon}_{est}$ is the strain rate of tensile steel reinforcemnts; $\dot{\varepsilon}_{esc}$ is the strain rate of compressive steel reinforcements; $\bar{x}$ is the netural axis depth (Fig. 4(c)); d is the effective depth that equals the distance from the centroid of tensile steel reinforcements to the extreme compression fiber; d' is the distance from the centroid of compressive steel reinforcements to the extreme compression fiber. During the impact process, the parameters $\dot{u}$ and $\bar{x}$ in Eqs. (9)–(11) are variables. The netural axial depth $\bar{x}$ changes slightly after yielding. On the other hand, the dynamic increase factors DIF_c and DIF_s are not sensitive to the changes of the parameter $\dot{u}$ for low-velocity impacts because of the logarithmic relationships (e.g., Eqs. (3) and (4)) between the dynamic increase factors and the strain rates of concrete and reinforcing steel. Hence, for simplification, the netural axial depth $\bar{x}$ corresponding to the yielding point and the average impact velocity ($\dot{u} = 1/2V_0$) were employed to estimate the nominal dynamic increase factors for concrete and reinforcing steel. In addition, although the velocity changed along the beam span, the change in velocity had a limited influence on the dynamic increase factor and the impact responses, as demonstrated in Section 5. Thus, like [6,28,34,35], the midspan cross-section was assumed to be representative for all beam cross-sections when approximately including the strain-rate effects.

2.4. Validations of the proposed model

All impact tests (a total of 12 reinforced concrete beams) presented by Fujikake et al. [6] were used to demonstrate the rationality of the proposed modeling method described above. Beams are normally attached to slabs in building or decks in bridges. Strictly speaking, impact tests on beams cannot represent real-world cases. However, compared with the tests on columns, many more tests on beams were carried out.

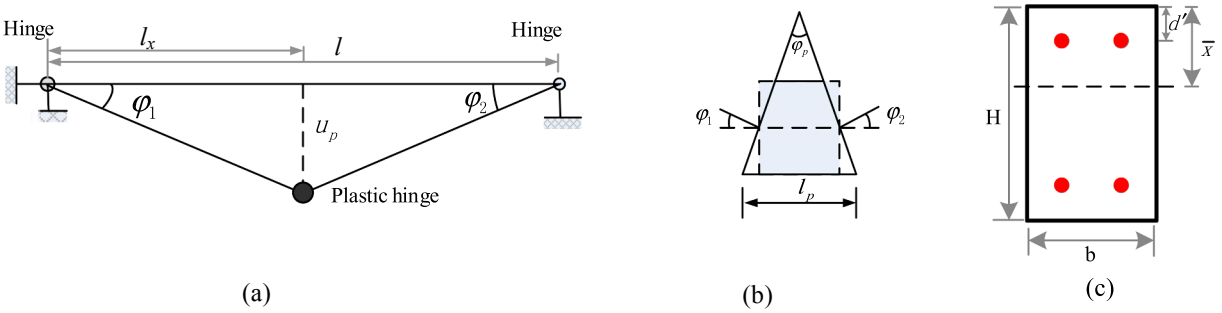

Fig. 4. (a) Plastic deflections of the beam with a concentrated plastic hinge; (b) schematic representation of the plastic hinge; (c) cross-section of a doubly reinforced concrete beam.

Table 1
Summary of impact tests.

Reference	NO.	ID	Geometry			Concrete strength $f_c^{'}$ (MPa)	Longitudinal bars			Transverse bars			Drop hammer	
			b(d) (mm)	h(d) (mm)	Span (m)		Diameter (mm)*	Ratio (%)	f_{sys}(MPa)*	Diameter (mm)	Ratio (%)	f_{sys} (MPa)	Mass (kg)	Velocity (m/s)
Fujikake et al. [6]	1	1322–0.3	150	250	1.4	42	13(22)	2.4	397(418)	10	1.4	295	400	2.42
	2	1322–0.6	150	250	1.4	42	13(22)	2.4	397(418)	10	1.4	295	400	3.43
	3	1322–1.2	150	250	1.4	42	13(22)	2.4	397(418)	10	1.4	295	400	4.85
	4	1322–2.4	150	250	1.4	42	13(22)	2.4	397(418)	10	1.4	295	400	6.85
	5	1616–0.15	150	250	1.4	42	16	2.1	426	10	1.4	295	400	1.71
	6	1616–0.3	150	250	1.4	42	16	2.1	426	10	1.4	295	400	2.42
	7	1616–0.6	150	250	1.4	42	16	2.1	426	10	1.4	295	400	3.43
	8	1616–1.2	150	250	1.4	42	16	2.1	426	10	1.4	295	400	4.85
	9	2222–0.3	150	250	1.4	42	22	4.1	418	10	1.4	295	400	2.42
	10	2222–0.6	150	250	1.4	42	22	4.1	418	10	1.4	295	400	3.43
	11	2222–1.2	150	250	1.4	42	22	4.1	418	10	1.4	295	400	4.85
	12	2222–2.4	150	250	1.4	42	22	4.1	418	10	1.4	295	400	6.85
Zhao [45]	13	D-1700	200	500	3	33	20(16)	1.66	495	6	0.188	345	1700	4.6
	14	D-1300	200	500	3	25	20(16)	1.66	495	6	0.188	345	1300	5.56
	15	D-868	200	500	3	25	20(16)	1.66	495	6	0.188	345	868	7.14
	16	C-1700	200	500	3	32	20(16)	1.66	495	6	0.094	345	1700	4.6
	17	C-1300	200	500	3	30	20(16)	1.66	495	6	0.094	345	1300	5.56
	18	C-868	200	500	3	26	20(16)	1.66	495	6	0.094	345	868	7.14
Xu and Zeng [51]	19	BD1	150	310	1.86	28	16	1.45	477	5.59	0.22	550	253	4.15
	20	BD2	150	310	1.86	27	16	1.45	477	5.59	0.22	550	253	7.11
	21	BD3	150	310	1.86	27	16	1.45	477	5.59	0.22	550	253	11.96
	22	BD4	150	310	1.86	41	16	1.45	477	5.59	0.22	550	578	7.81
	23	BD5	150	310	1.86	41	16	1.45	477	5.59	0.22	550	578	5.1
Saatci et al. [8]	24	SS1a-1	250	410	3	45	30	2.75	464	7.01	0.1	605	211	8
	25	SS2a-1	250	410	3	47	30	2.75	464	7.01	0.2	605	211	8
	26	SS3a-1	250	410	3	47	30	2.75	464	7.01	0.3	605	211	8
	27	SS1b-1	250	410	3	45	30	2.75	464	7.01	0.1	605	600	8
	28	SS2b-1	250	410	3	47	30	2.75	464	7.01	0.2	605	600	8
	29	SS3b-1	250	410	3	47	30	2.75	464	7.01	0.3	605	600	8
Demartino et al. [9]	30	FL1	330	330	1.6	28	8	0.9	427	6.5	0.3	416	1582	2.25
	31	FL2	330	330	1.6	28	8	0.9	427	6.5	0.09	416	1582	2.25
	32	FM1	330	330	1.6	28	8	0.9	427	6.5	0.3	416	1582	3
	33	FM2	330	330	1.6	28	8	0.9	427	6.5	0.09	416	1582	3
	34	FH1	330	330	1.6	28	8	0.9	427	6.5	0.3	416	1582	4.5
	35	FH2	330	330	1.6	28	8	0.9	427	6.5	0.09	416	1582	4.5
Liu et al. [7]	36	E1F0	200	200	1.4	30	8	1.92	418	6	1.3	427	442	4.84
	37	E2F0	200	200	1.4	30	8	1.92	418	6	1.3	427	568	6.85
	38	E1F2	200	200	1.4	30	8	1.92	418	6	1.3	427	442	4.84
	39	E2F2	200	200	1.4	30	8	1.92	418	6	1.3	427	568	6.85
	40	E1F3	200	200	1.4	30	8	1.92	418	6	1.3	427	442	4.84
	41	E2F3	200	200	1.4	30	8	1.92	418	6	1.3	427	568	6.85
	42	E2F0S1	200	200	1.2	30	8	1.92	418	6	1.3	427	568	6.85
	43	E2F3S1	200	200	1.2	30	8	1.92	418	6	1.3	427	568	6.85
	44	E2F0S2	200	200	1	30	8	1.92	418	6	1.3	427	568	6.85
	45	E2F3S2	200	200	1	30	8	1.92	418	6	1.3	427	568	6.85
	46	E1F3L6	200	200	1.4	30	8	0.96	418	6	0.72	427	442	4.84
	47	E2F3L6	200	200	1.4	30	8	0.96	418	6	0.72	427	568	6.85

* Note. The number in bracket means two types of longitudinal steel bars in the specimen.

Hence, the tests on beams as the useful supplements were employed to address the impact resisting mechanisms and to validate the proposed modeling method. Further impact tests on beams with slabs or decks are worth conducting in the future. For all beam specimens, the cross-sectional dimensions are 150 mm in width and 250 mm in depth, and the clear span length is 1400 mm. Sufficient amount of transverse reinforcements were arranged to ensure that all specimens are flexure-critical. Parameters varied in these impact tests on the reinforced concrete beams included: longitudinal reinforcement (i.e., three different series: S1616, S1316 and S2222) and drop heights (i.e., four different heights: 0.15 m, 0.3 m, 0.6 m and 1.2 m for Series S1616; and 0.3 m, 0.6 m, 1.2 m and 2.4 m for Series S1322 and S2222). Details of the specimens are presented in Fig. 1(a) and (b). Table 1 lists the material properties of the specimens and the impact events. More details on these impact tests can be found in Fujikake et al. [6]. The FE models of the beams were developed using the proposed method shown in Fig. 1.

The predicted results including impact responses including impact forces and impact-induced midspan deflections, and failure modes are shown in Figs. 5–7 along with the experimental data. Generally, the numerical results are in good agreement with the experimental results particularly when only overall flexural failures occur in the impacted beam, indicating the applicability of the proposed modeling method. Similar to the analytical results provided in Fujikake et al. [6], the midspan deflections obtained from the proposed methods are larger than the experimental data for the specimens with severe local damage near the impact loading point (Fig. 6(h) and (l)). These differences are attributed to the fact that the local damage cannot be well captured when using elastic spring to model the interaction between the drop hammer and the RC beam. To improve the numerical models, the elastic spring presented in Section 2.2 was tentatively replaced with an inelastic spring to account for the influence of the local damage around

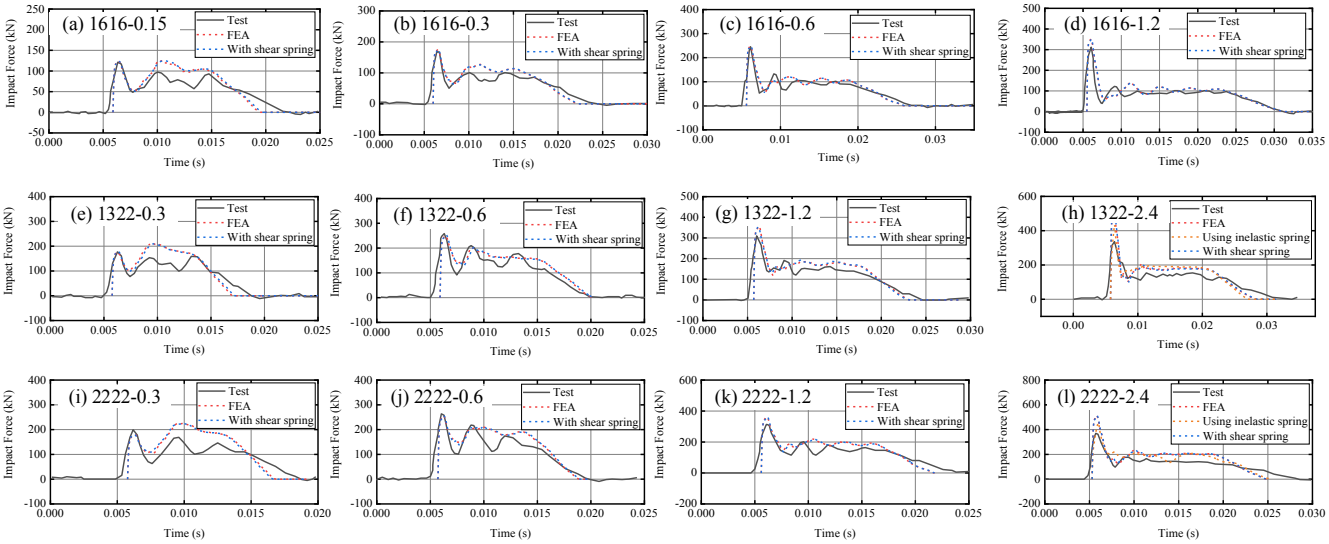

Fig. 5. Comparisons of impact forces between the experiments [6] and the FE simulations (Note: "1616-0.15" means that the tested beam is Series 1616 in Fujikake et al. [6] and the drop height is 0.15 m).

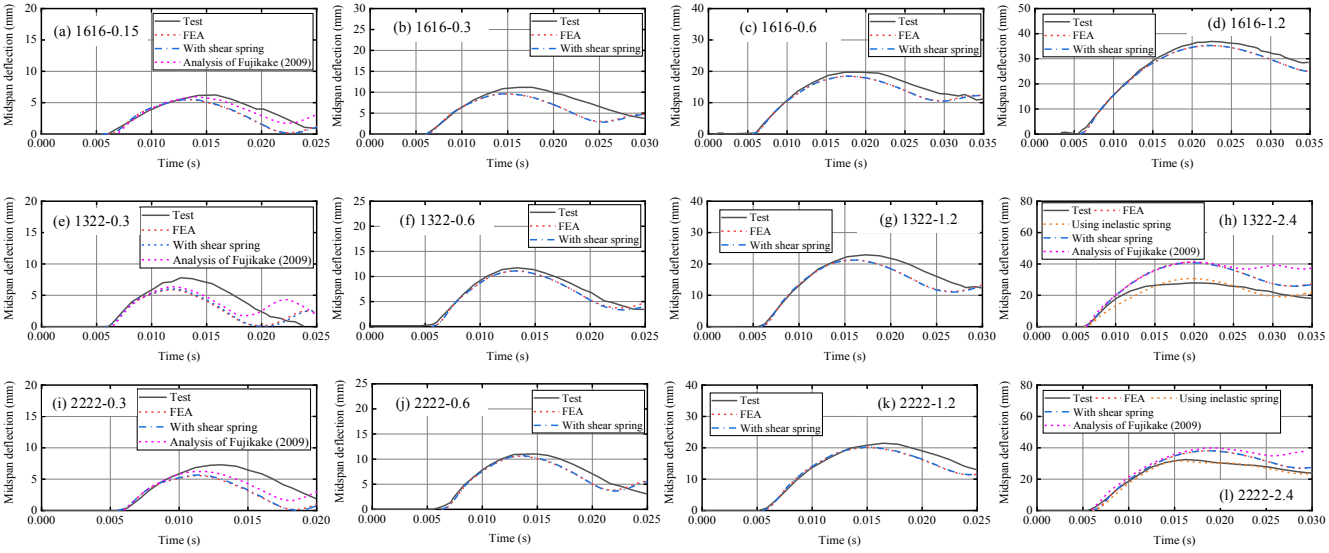

Fig. 6. Comparisons of midspan deflection responses between the experiments [6] and the FE simulations.

the impact point. The force-deformation relation of the inelastic spring is presented in Fig. 2(a) using a dotted line. The point *Co* corresponds to the depth of the concrete cover. As shown in Fig. 6(h) and (l), better agreements were achieved between the experimental and numerical midspan deflection responses of Series 1322 and S2222. Compared to the analytical model presented in Fujikake et al. [6], the proposed method is able to obtain the whole deformation and the internal force along the beam (see Fig. 7).

For impact case S2222-0.3 (Fig. 5(i)), the maximum impact force (~223.0 kN) predicted from the proposed model is greater than the experimentally-measured force (~169.0 kN) at the same instant (i.e., t = 9.8 ms). The previous studies [7,36] pointed out that the impact-force time histories observed from the tests can be characterized by four different phases: peak-force wave (or initial contact) phase (Phase I), loading phase (Phase II), unloading phase (Phase III), and free vibration phase (Phase IV). Typically, Phase I ends when the hammer and the impacted specimen at the contact point have approximately the same speeds (just like stick together). During the loading phase (Phase II), the hammer speed is roughly the same as that of the contact point of the beam [36]. Hence, the loading phase (Phase II) of the drop-hammer impact test usually behaves like the rapid loading test reported in the same reference [6]. The impact force in the loading phase should be approximately equal to that measured from the rapid loading tests. In this case, the midspan deflection of the beam is 5.5 mm (Fig. 6(i)) at the time corresponding to the maximum impact force at Phase II. According to the load-midspan deflection relations (Fig. 3) measured from the quasi-static and rapid loading tests, the corresponding beam resistances are 185.0 kN and 222.0 kN, respectively. Therefore, the maximum impact force in Phase II should be near 222.0 kN, and not less than 185.0 kN (quasi-static case). However, the impact force measured from the impact test was 165.0 kN, which was not only less than the rapid loading test result (222.0 kN) but also less than the quasi-static loading test result (185.0 kN). This implies that there is a contradiction between the drop-hammer impact test and the rapid loading test reported in the same Ref. [6]. The inconsistency may be attributed to the possible uncertainty such as material properties and manufacturing errors of the beam specimen in tests. For example, if the concrete cover of the beam specimen is thicker than the design value to some extent, the resistance (capacity) of the beam specimen and the impact force would be lower than the expected value during impact testing.

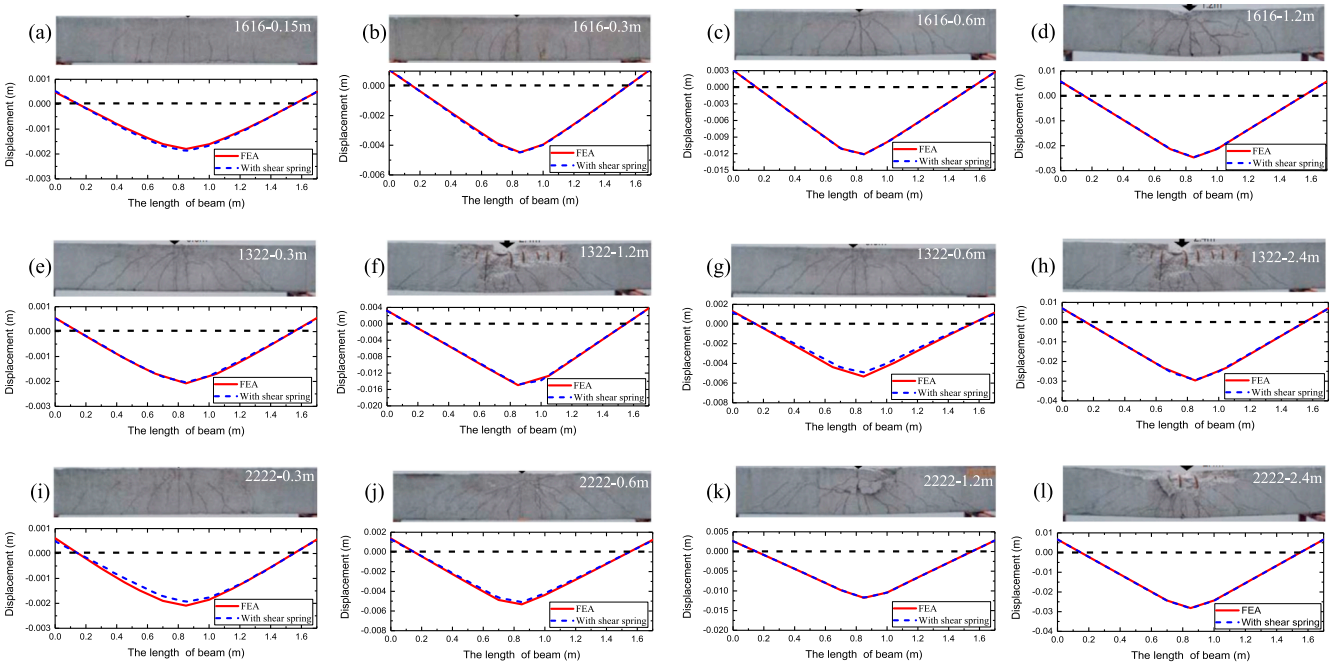

Fig. 7. Comparisons of failure modes between the experiments [6] and the FE simulations.

3. Modeling of shear failure in RC members

The shear effects have little impacts on the flexure-critical reinforced concrete members under impact loading, as shown in the above simulation results. However, the previous experimental studies [8] indicated that shear failures could be observed in RC beams and columns subjected to impact loading, even though these members tend to fail in a flexural-dominated manner under static loading. Therefore, it is essential to incorporate an appropriate modeling method in the fiber-based nonlinear beam-column element models to accurately and efficiently capture impact-induced shear effects. For seismic analysis, one of typical approaches is placing a shear spring in series with flexural beam-column elements to simulate the behavior of shear-critical RC members. This approach has been widely used because it is straightforward and easy for use in the evaluation of seismic behavior [37–39]. The method was extended in this study to consider shear effects for the reinforced concrete members subjected to low-velocity impact loading.

3.1. Impact-induced shear failures and modeling

Yi et al. [40] pointed out that two main types of shear cracks can be observed from the impact tests on RC beams: (1) inclined cracks in the shear span that are similar to cracks under static loads (Type I); (2) diagonal cracks forming a shear plug (like a punching shear failure) near the contact-impact point (Type II). Fig. 8 schematically shows these two types of shear cracks under impact loads. Compared to shear responses due to earthquake excitations, punching shear failures would be unique to the impact behaviors of RC members. For this reason, two different types of shear springs were added into the nonlinear beam-column element models to simulate impact-induced shear responses, as illustrated in Fig. 9(a). Specifically, zero-length spring elements in OpenSees were employed to capture the impact-induced shear responses. A uniaxial hysteretic material model that governs the behavior of the spring was used to describe nonlinear shear strength characteristics (i.e., shear strength versus shear deformation relationships) of RC members.

3.2. Shear capacity curves

Much research has been devoted to quantifying shear strengths of reinforced concrete beams and columns under static loads in the past over 100 years [41]. Numerous equations have been prescribed in various current design codes of building and bridge structures to evaluate shear strengths. Compared to the studies on static shear strengths, relatively fewer studies placed emphasis on addressing the shear strengths of RC members under dynamic loads. Adhikary et al. [42] performed the physical experiments to examine the dynamic behavior of RC deep beams under varying rates of concentrated loading and indicated that the dynamic shear strength significantly exceeds the static one. Hence, strain-rate effects, which are often omitted in seismic analysis, need be taken into account when shear strengths are evaluated for impact simulations. On the other hand, to define the shear springs in the proposed model (Fig. 9), not only the shear strength but also the relationship between shear force and deformation should be provided. The existing relations between shear force and deflection for seismic analysis (e.g., in [37–39]) are not applicable to impact simulations, because particular features (e.g., shear strength degradation) related to cyclic loading have to be mainly considered in the seismic analysis.

A nonlinear finite element program VecTor2 has been developed by Prof. Vecchio's group at the University of Toronto for accurately predicting the inelastic response (particularly shear response) of two-

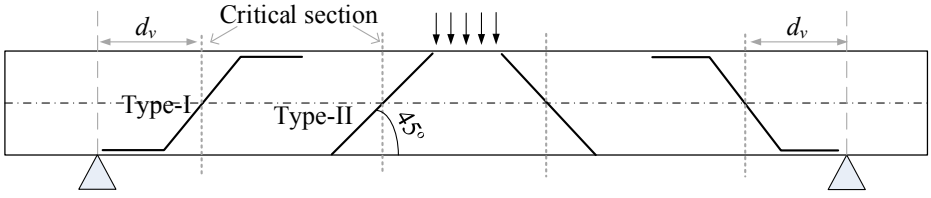

Fig. 8. Shear failure modes of RC beams under impact [40].

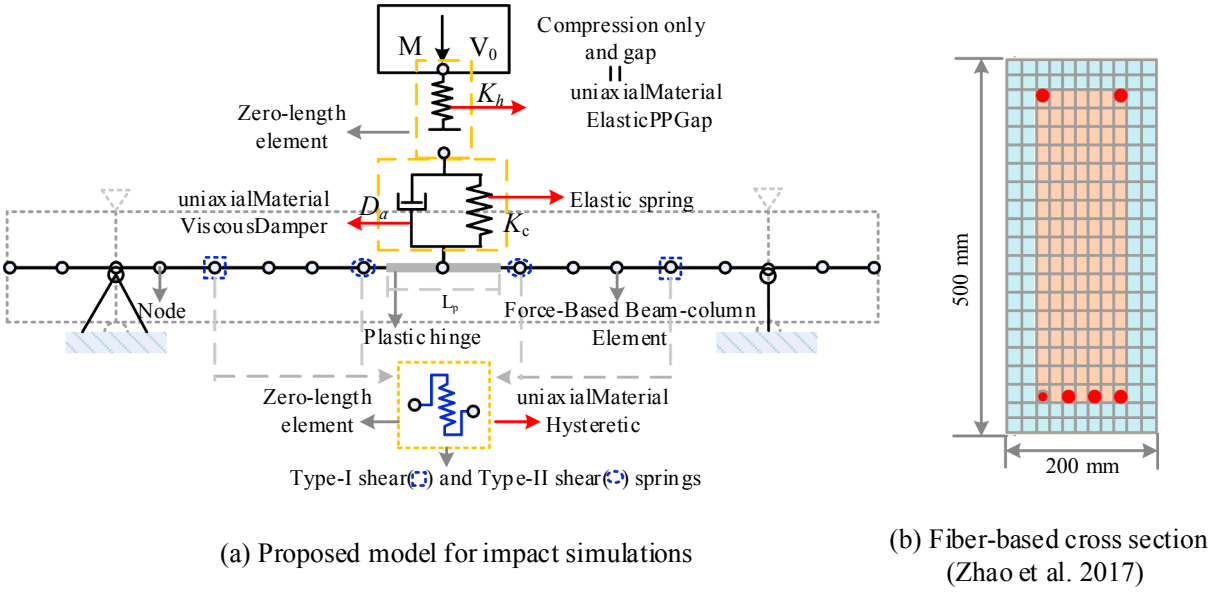

(a) Proposed model for impact simulations

(b) Fiber-based cross section (Zhao et al. 2017)

Fig. 9. Proposed models with shear springs.

dimensional reinforced concrete membrane structures since 1990 [43,44]. The finite element code is based on the Modified Compression Field Theory (MCFT) that uses a smeared, rotating-crack formulation [43] and the Disturbed Stress Field Model [44]. Validated against a large number of experimental tests (over 1000 tests), VecTor2 has been demonstrated as capable of predicting both flexure- and shear-deformation responses of a variety of RC members subjected to monotonic, cyclic and reverse cyclic loads. Also, the strain-rate effects of concrete and reinforcing steel can be modeled in VecTor2 to consider the influences of loading rates on the capacity of RC members under dynamic (impact) loading. For these reasons, VecTor2 was employed in this study to estimate shear capacity curves (i.e., the relationship between shear force and deformation) for the two types of shear springs in Fig. 9(a).

Take the reinforced concrete beams tested performed by Zhao et al. [23,45] (Fig. 9) as an example for illustrating how to evaluate shear capacity curves using VecTor2. Fig. 10(a) and (b) present the VecTor2 models for the beams with the Type-I shear failure and the Type-II shear failure illustrated in Fig. 8, respectively. Because impact loads were applied at the midspan of the RC beams with symmetric details and reinforcements, only half of the beam span was modeled in Fig. 10. Eight-DOF rectangular elements with a mesh size of 25 × 20 mm in X- and Y-directions, respectively, were used to model the reinforced concrete. Four-DOF truss elements were employed to model the longitudinal reinforcing bars. The transverse reinforcement was smeared within the concrete. The loading plate was modeled with rigid continuum elements. Bearing elements with unidirectional stiffness were used to model the interface between the load plate and the concrete elements to provide a more reasonable representation of the force distribution around the loading point [46]. For the Type-I shear failure, it is assumed that the shear capacity can be estimated by the membrane model (Fig. 10(a)) with the same shear span (e.g., 3 m in the tests conducted by Zhao et al. [23,45]) as the impacted beams. For the Type-II shear failure, Zhao et al. [23,45] pointed out that the shear cracks were inclined at an angle of about 45 degrees with respect to the longitudinal axis of the RC members. Also, these shear cracks were typically developed when inertia-related effects were significantly pronounced. Such influences can be roughly equivalent to the reduction in shear spans. In this case, the impacted beam behaved like a deep beam as shown in Fig. 10(b) with an equivalent span, which can be estimated as

$$L_2 = 2H + W_h \tag{12}$$

where H is the height of the impacted beam; W_h is the width of the impacting object (e.g., drop hammer).

Five different loading rates (i.e., 0.5 m/s, 2 m/s, 4 m/s, 6 m/s and 8 m/s) were investigated to evaluate the influence of loading rates on the shear force-deformation responses. For the Beam *C* and Beam *D* in Zhao et al. [23,45], Fig. 11 shows the applied force versus deformation curves obtained from the VecTor2 models for the two types of shear failures. It can be seen that the loading rates have a minor influence on the upward portion of the force-deformation curves. On the contrary, the descending (or softening) branches of the force-deformation curves were significantly affected by the loading rates. For the conservative and convenient considerations, the dashed lines (as shown in Fig. 11) can be chosen to describe the force-deformation relationships of RC beams. It is worth noting that the total deformations in these numerically-obtained results include not only the shear deformation but also the flexural deformation resulted from bending moments. Only if the flexural deformations are excluded from these curves, they can be used to define the shear springs in Fig. 9. Shear deformations are usually very small for Point (a) in the force-deformation curves. In this case, an approximately linear relationship between the shear force and the resulting deformation can be assumed. The initial slope of the curve would be the initial shear stiffness. Accordingly, the initial shear stiffness(K_g) and the corresponding shear deformation (D_{a_1})at Point (a_1) in Fig. 11(a) can be expressed as

$$K_g = GA/L \;\; D_{a_1} = F_{sa}/K_g \tag{13}$$

where G is the shear modulus; A is the shear area of beam cross-section; L is the shear span or the support length; F_{sa} is the shear force at the Point (a). Similarly, Point (b) in the dashed blue curve corresponds to Point (b_1) in the shear capacity curve (i.e., the solid red[1] curve in Fig. 11) that excludes the flexural deformation. The shear deformation D_s at Point (b_1) is equal to that the total deformation D_t substracts the corresponding flexural deformation D_f, which can be writted as

$$D_s = D_t - D_f = D - D_{fs} + F_{sb}/K_g \tag{14}$$

where F_{sb} is the shear force at Point (b); D_{fs} is the combined deformation corresponding to the applied force F_{sb} in the flexural curve. The

[1] For interpretation of color in Fig. 11, the reader is referred to the web version of this article.

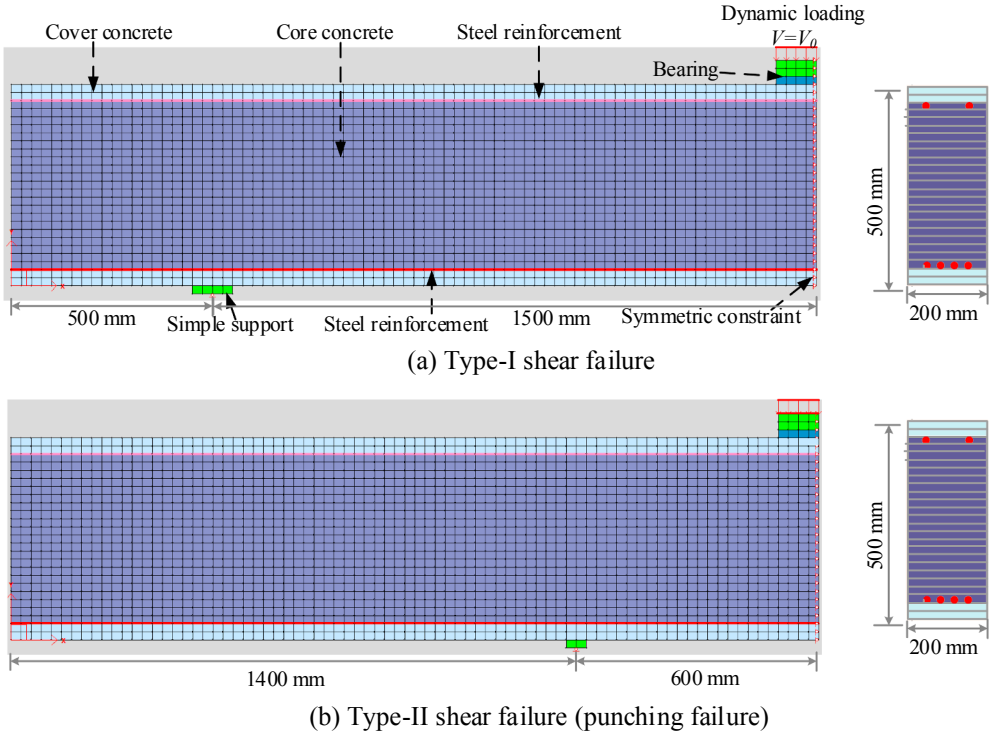

Fig. 10. VecTor2 models for predicting shear capacity curves.

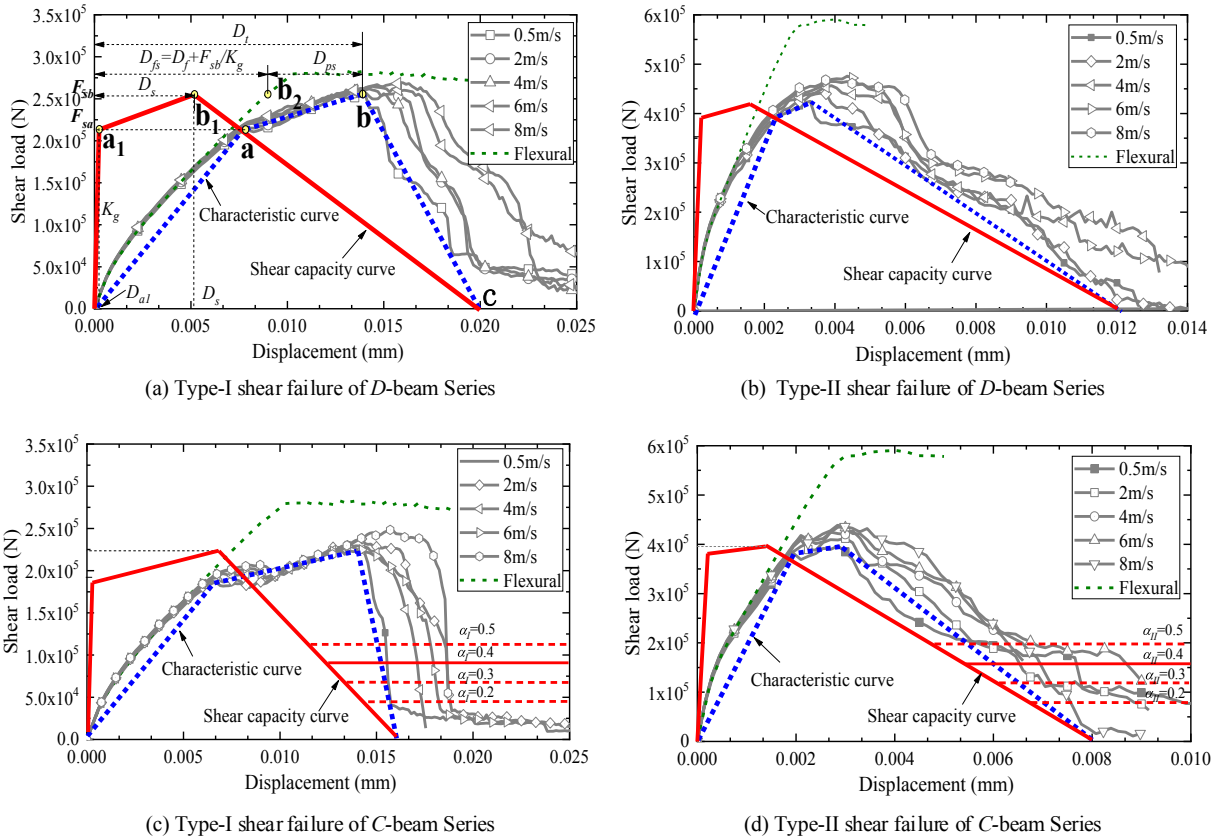

Fig. 11. Shear capacity curves calculated by VecTor2 models.

determination of D_s is illustrated in Fig. 11(a). In terms of Point (c), $D_s = D_t$ because the combined deformation and the applied force are zero in the flexural curve in this case.

Based on the above procedure, the original force-deformation responses obtained from the VecTor2 (membrane) models can be converted into the shear capacity curves (e.g., the solid red curve in Fig. 11) that are required for the definition of the shear springs in the proposed models (e.g., Fig. 9). It is worth mentioning that two kinds of

Table 2
Locations of Type-I shear cracks.

Reference	Specimen	H (cm)	D1	D2	D1/H	D2/H
Zhao [45]	C-1700	50	50	65	1	1.3
	C-1300	50	50	50	1	1
	C-868	50	50	–	1	–
	D-1700	50	62	50	1.24	0.81
	D-1300	50	60	–	1.20	–
	B-1700	50	58	65	1.16	1.12
	B-1300	50	70	–	1.40	–
	B-1052	50	55	45	1.10	0.82
Xu and Zeng [51]	DB1	31	22	–	0.71	–
	DB2	31	31	–	1	–
	DB5	31	28	42	0.90	1.4
Saatci et al. [8]	SS0a	41	47	–	1.15	–
	SS0b	41	47	–	1.15	–
	SS1b	41	35	–	0.855	–
	SS2b	41	47	–	1.15	–

capacity curves associated with both flexural and shear failures need to be determined. For example, shear failures usually occur in the membrane model (e.g., Fig. 10(a)) during the punching shear failure analysis (Type II). The flexural capacity curve cannot be directly derived from the identical membrane model when shear failures occur in the membrane models created according to specimen details. In this case, the subsidiary flexural capacity curves would be estimated from the adjusted membrane model, in which shear reinforcements are added to ensure the presence of the flexural-dominated failure. Usually, longitudinal reinforcements are dominated for the flexural behavior, while the influences of shear reinforcements can be omitted [47–49]. On the contrary, longitudinal reinforcements would be suitably increased in the membrane model to obtain the force-deformation responses associated with shear-dominated failures when flexural-dominated failures appear in the original membrane model. Although these changes might have somewhat effects on structural capacity curves, their influences are usually minimal in comparison with the dominated factors.

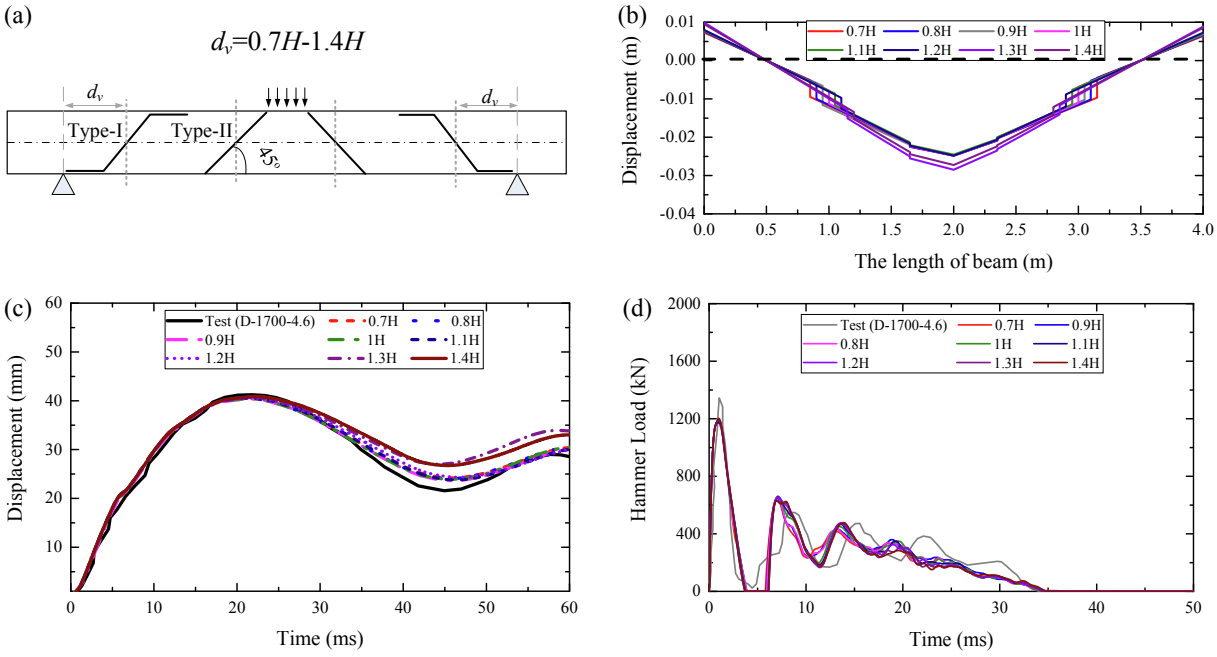

Fig. 12. The influence of shear springs on Type-I shear cracking behaviors.

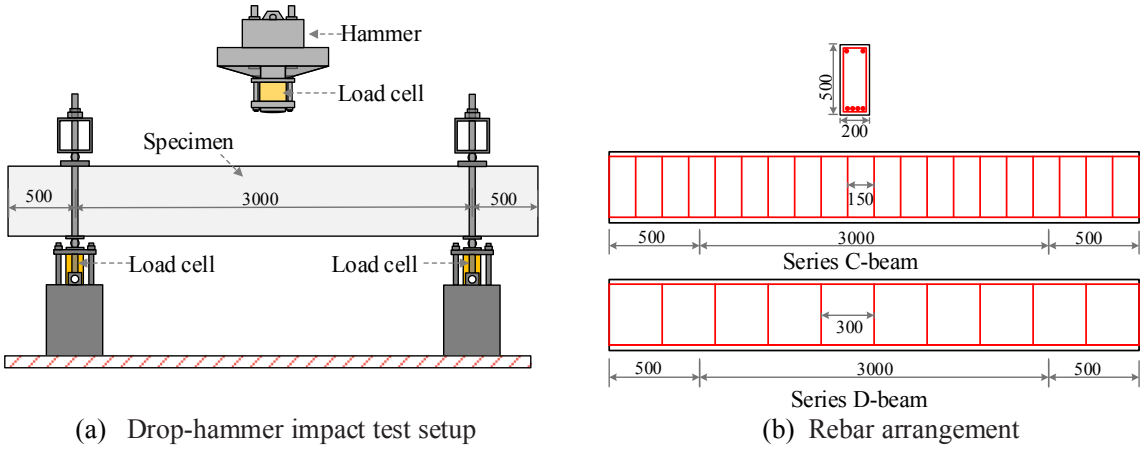

Fig. 13. Drop-hammer impact tests conducted by Zhao et al. [45] (Unit: mm).

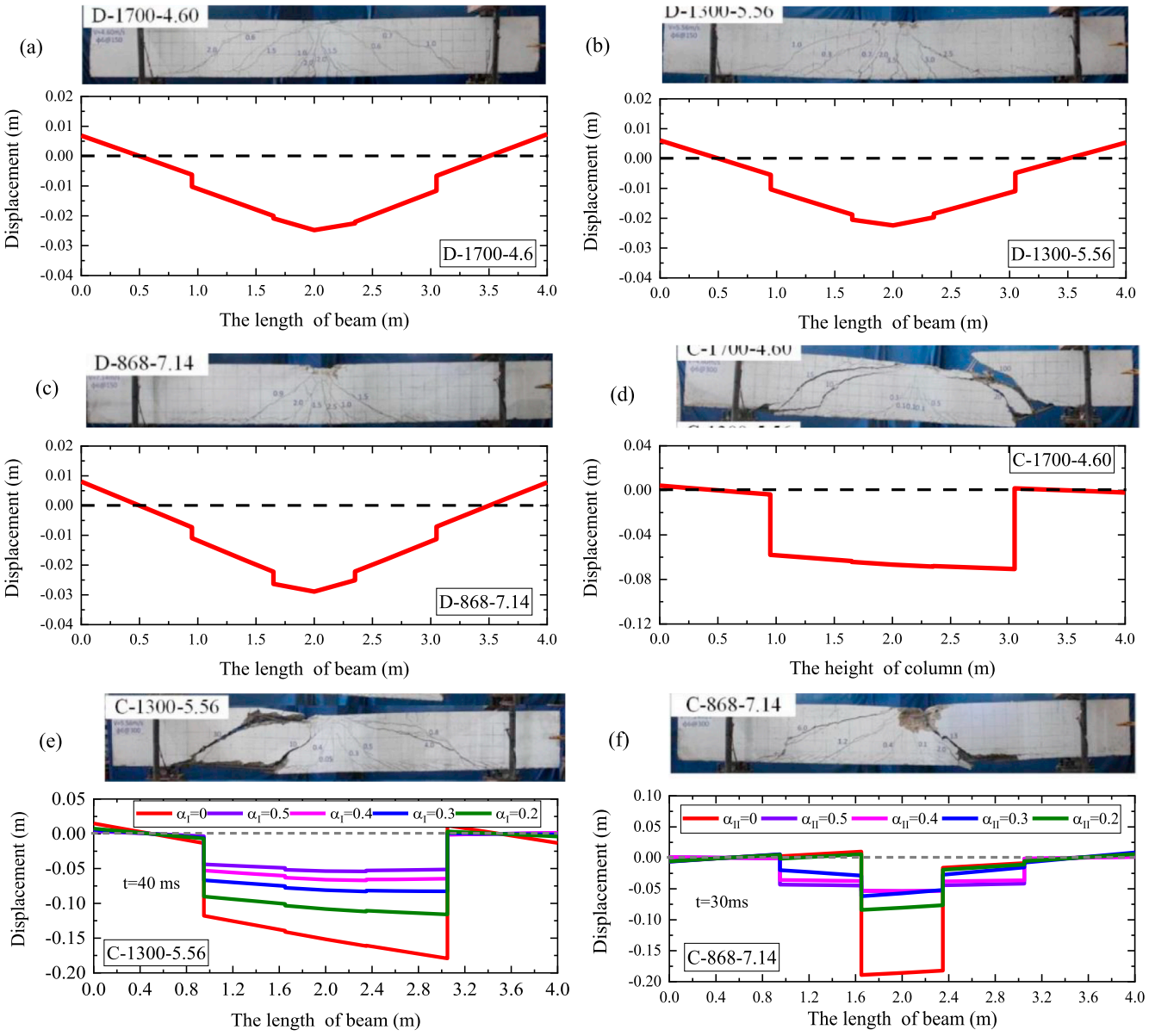

Fig. 14. Comparisons of failure patterns between the experiments [45] and the FE simulations.

3.3. Locations of shear springs

Based on the experimental observations [23,45], it is easy to determine the location of the shear spring in the fiber-based nonlinear beam-column element models for the punching shear failure (i.e., Type II shear failure). As illustrated in Figs. 8 and 9, the shear springs were coupled in the critical sections located at the crossing point between the inclined crack and longitudinal central axis (i.e., $H + W_h/2$ away from the contact-impact point).

For the Type-I shear cracks, the positions of the main cracks in the fifteen beams after impact were examined and summarized in Table 2. It can be found that the distance d_v of the shear cracks away from the support ranged from $0.7H$ to $1.4H$. The drop hammer impact test on the specimen D-1700 in [23,45] was simulated to evaluate the influence of the parameter d_v on impact-induced responses. In the numerical simulations, the parameter d_v varied from $0.7H$ to $1.4H$, as shown in Fig. 12(a). Fig. 12(b)–(d) present the numerically-obtained beam deflections over the beam span and time histories of midspan displacements and impact forces along with the experimental data, respectively. Good agreements were always achieved for the midspan displacements and the impact forces between the experimental and numerical results when the parameter d_v varied from $0.7H$ to $1.4H$ (see Fig. 12(c) and (d)). This implies that the parameter d_v has a limited influence on the impact-induced responses. Fig. 12(b) shows that the shear deformation slightly increases with the decrease of the parameter d_v. In other words, the relatively low value of d_v would lead to a conservative estimation of the shear failure. Because shear failures are brittle, the relatively conservative evaluation is preferable for structural safety. On the other hand, Bentz [50] recommended that the critical sections regarding the shear check are located at $0.9H$ and $0.75H$ for simply supported beams and the columns with rotation constraints at two ends, respectively. Therefore, for the simply supported beams and the columns with fixed ends, shear springs were placed in accordance with the suggestion of Bentz [50] to capture the responses related to the Type-I shear cracks. For other types of beams and columns, further studies should be conducted to examine the availability of these suggestions.

Based on the above discussions, the approach of the definition of shear springs, which was consistently used for all impact cases studied in this paper, can be summarized as

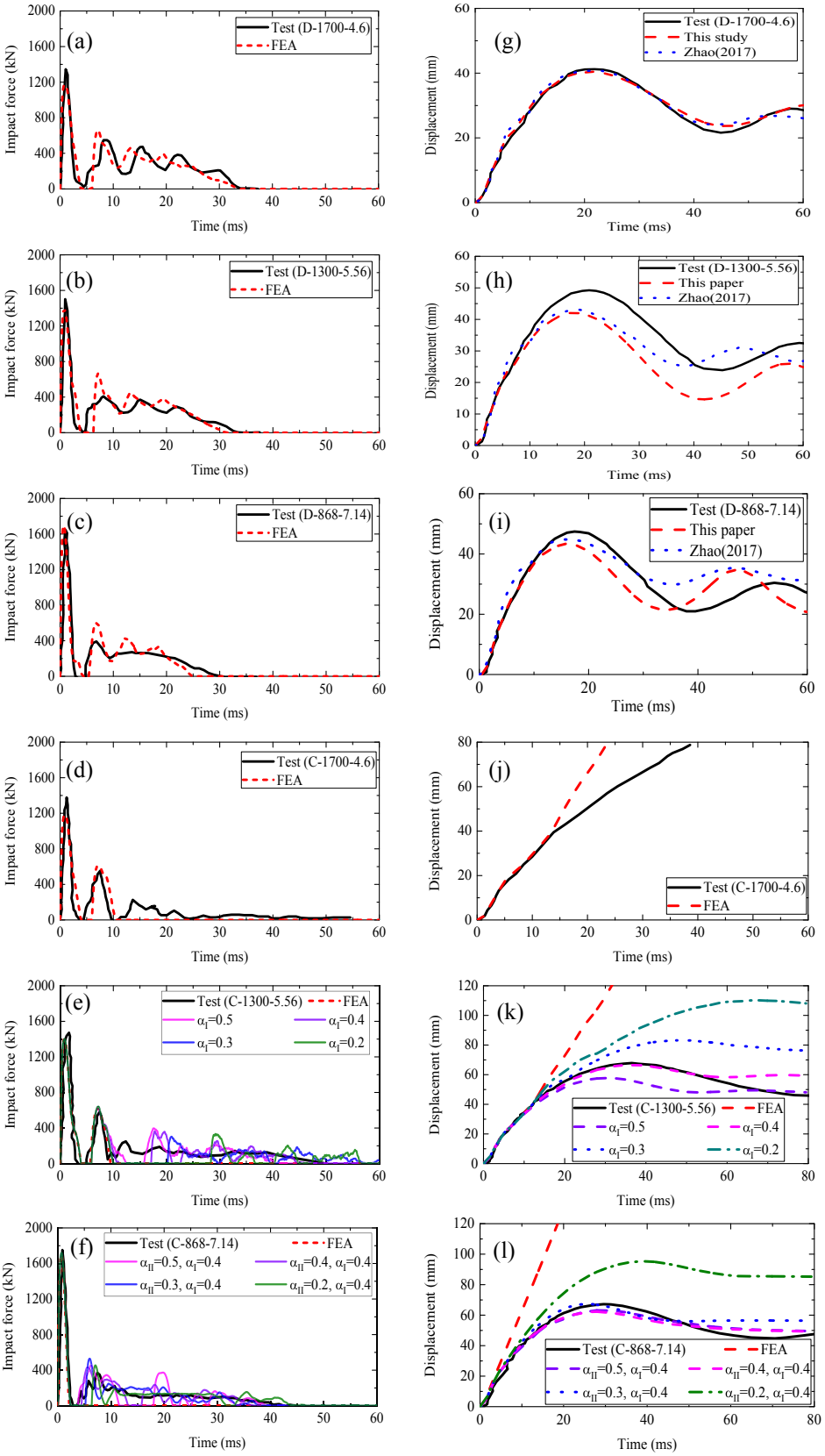

Fig. 15. Impact responses obtained from the experiments [45] and the FE simulations.

(1) Creating the membrane model using the program VecTor2 based on the structural geometry, materials, and reinforcements of the impacted RC members.

(2) Obtaining the capacity curve of Type-I shear springs. For conservative consideration, a relatively low constant velocity (e.g., 0.5 m/s) can be used applied at the contact-impact zone of the

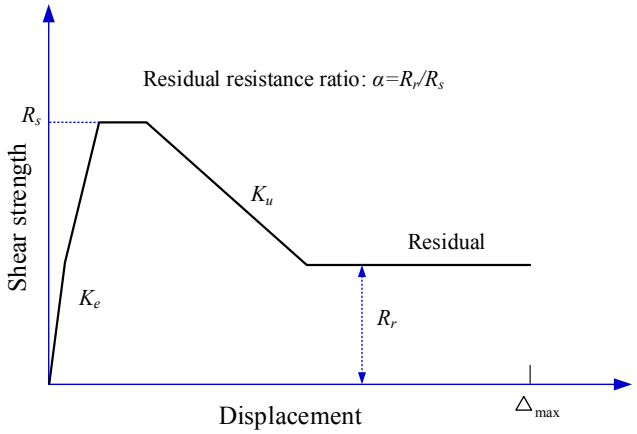

Fig. 16. Envelope curve of shear resistance [52].

membrane model to obtain the load-deformation curve. Based on Eqs. (13) and (14), the flexural deformations are excluded from the load-deformation curve to obtain the shear capacity curve.

(3) Obtaining the capacity curve of Type-II shear (punching) springs. In this case, only the shear span is modified by Eq. (12), and other definitions and treatments are the same as the above analysis for obtaining the capacity curve of Type-I shear springs.
(4) Assigning shear springs in nonlinear beam-column element models at the given locations as discussed above.

3.4. Validations of proposed method for shear

A total of 23 impact tests on RC members reported in [8,9,23,51] were used to verify the proposed FE model with shear springs. All of them exhibited shear damages in the impact tests.

3.4.1. Impact tests on RC beams conducted by Zhao et al. [23]

The drop-hammer impact tests on simply supported RC beams were recently performed by Zhao et al. [23,45], as shown in Fig. 13. Two different transverse reinforcement ratios (ρ_T = 0.094% for Series C-beam and 0.188% for Series D-beam) were investigated in the tests. The total length of the beam specimen was 4 m, and the clear span between the two supports was 3 m. All beam specimens had the same cross-sectional dimensions of 500 mm in depth and 200 mm in width. The

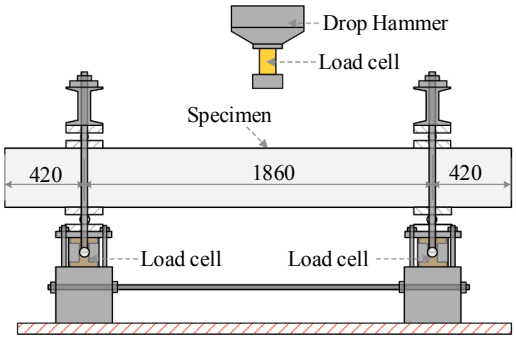

(a) Drop hammer impact test setup Zeng et al (2014)

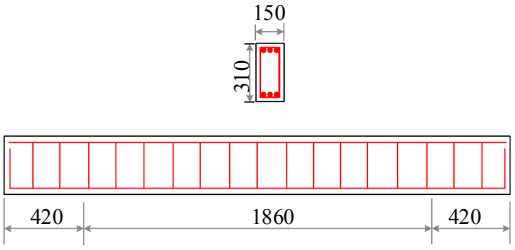

(b) Rebar arrangement (Unit: mm)

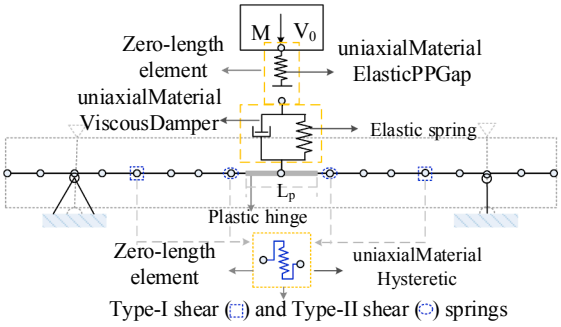

(c) Proposed model for impact simulation

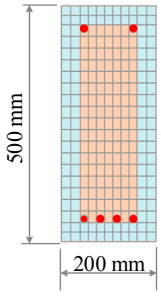

(d) Fiber section of beam element

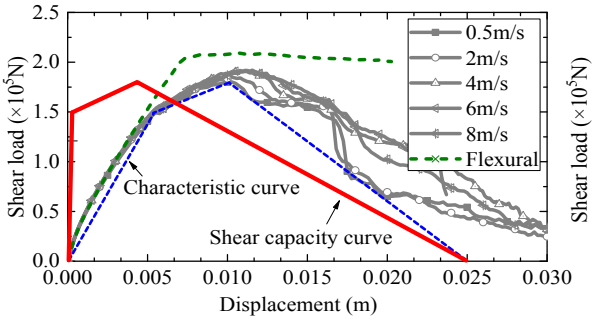

(e) Type-I shear failure

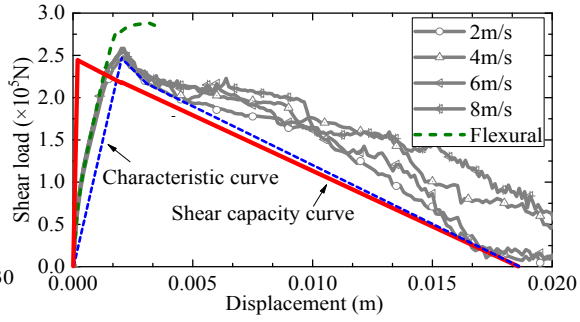

(f) Type-II shear failure

Fig. 17. Drop-hammer impact tests on RC beam conducted by Xu and Zeng [51].

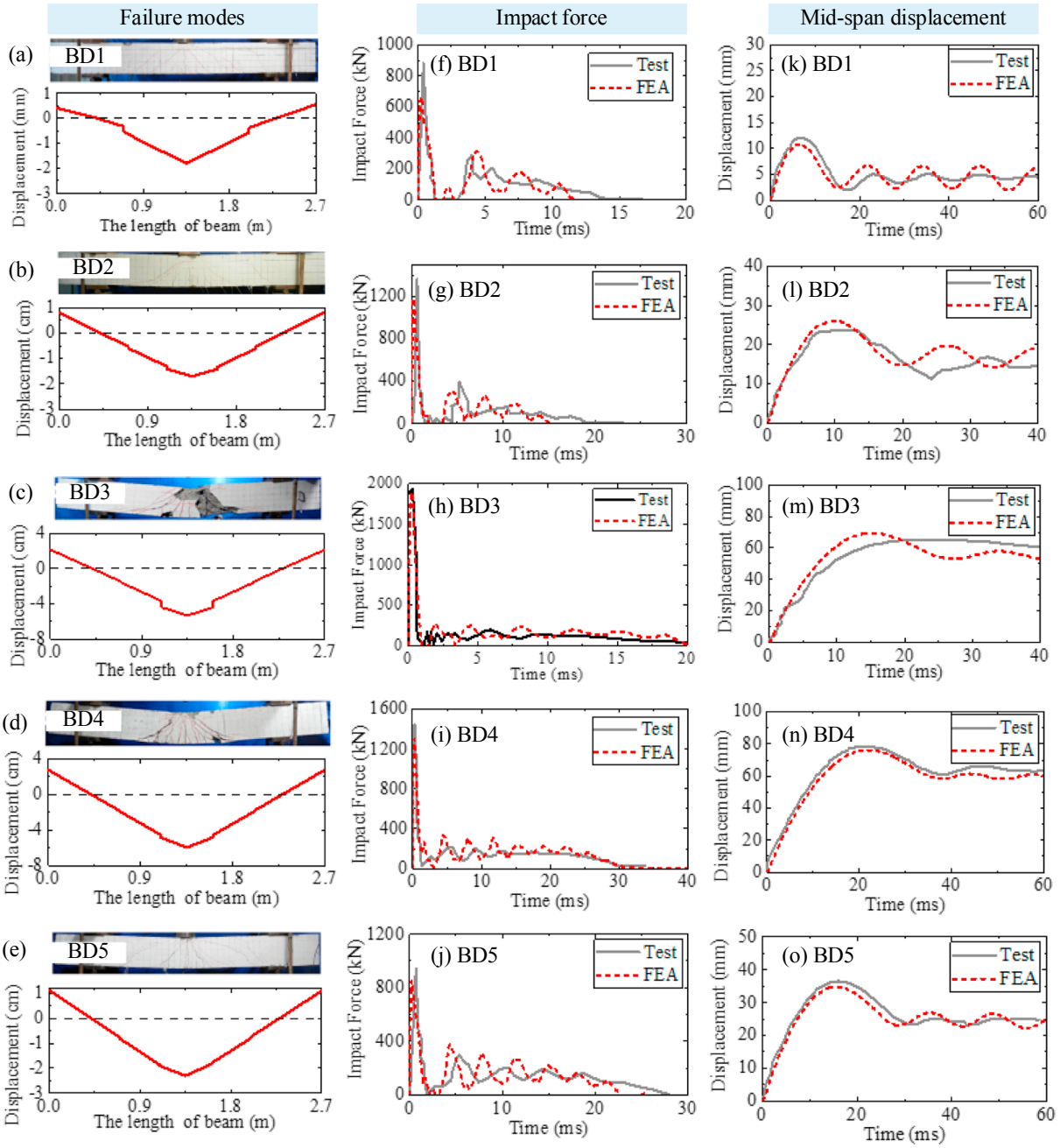

Fig. 18. Impact responses of the experiments [51] and the FE simulations.

longitudinal reinforcements consisted of two 16-mm diameter steel bars and four 20-mm diameter steel bars. According to the material properties given in [23,45], the uniaxial compressive strengths of the concrete used in the testing ranged from 20 MPa to 25 MPa, and the yielding strengths of the transverse reinforcement and the longitudinal reinforcement were 345 MPa and 495 MPa, respectively. The thickness of concrete cover was 30 mm for the longitudinal bars at the top and the bottom. The material properties of the specimens are summarized in Table 1. More detailed information on the tests can be found in Zhao et al. [23,45].

According to the above drop-hammer impact tests, the nonlinear beam-column model with shear springs was created, as illustrated in Fig. 9. Similar to the simulations of the impact tests by Fujikake et al. [6], $K_h = 1 \times 10^9$ N/m and the contact stiffness was estimated using the approach provided in [6] (i.e., $K_c = 5 \times 10^8$ N/m). Based on Eq. (8), $C_L = 2.68$. By using the above membrane models, the shear force-deformation responses of the two specimen series (Fig. 11) were obtained for the two types of shear cracks (failures) to define the shear springs in the nonlinear beam-column model.

The numerically-obtained results (e.g., deformation pattern after impact, midspan displacement and impact forces) are presented in Figs. 14 and 15 along with the corresponding experimental data. As shown in Fig. 14(a)–(c), the numerical simulations indicate that Series D-beam had the combined deformation patterns that include relatively large flexural deformation and some shear damages. These results are consistent with the experimental observations. For Series C-beam, shear-dominated failures were well predicted by the proposed numerical method, and the specific types of shear failures (Type I or Type II) agreed well with the experimental results, as shown in Fig. 14(d)–(f). This indicates that the proposed method is capable of capturing the failure modes of the RC beams under impact loading.

The midspan displacements of impact case D-1700-4.6 obtained

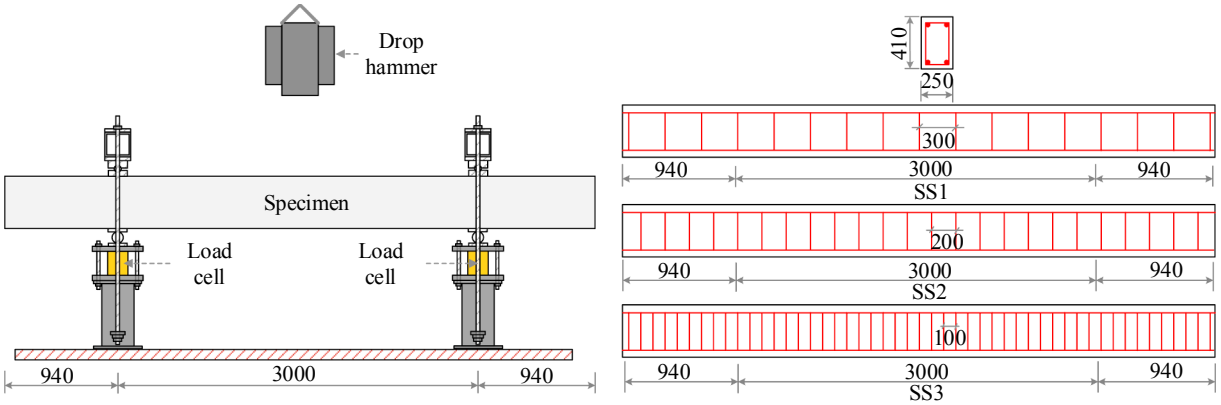

(a) Drop-hammer impact test setup (b) Rebar arrangement

Fig. 19. Drop-hammer impact tests on RC beams conducted by Saatci et al. [8] (Unit: mm).

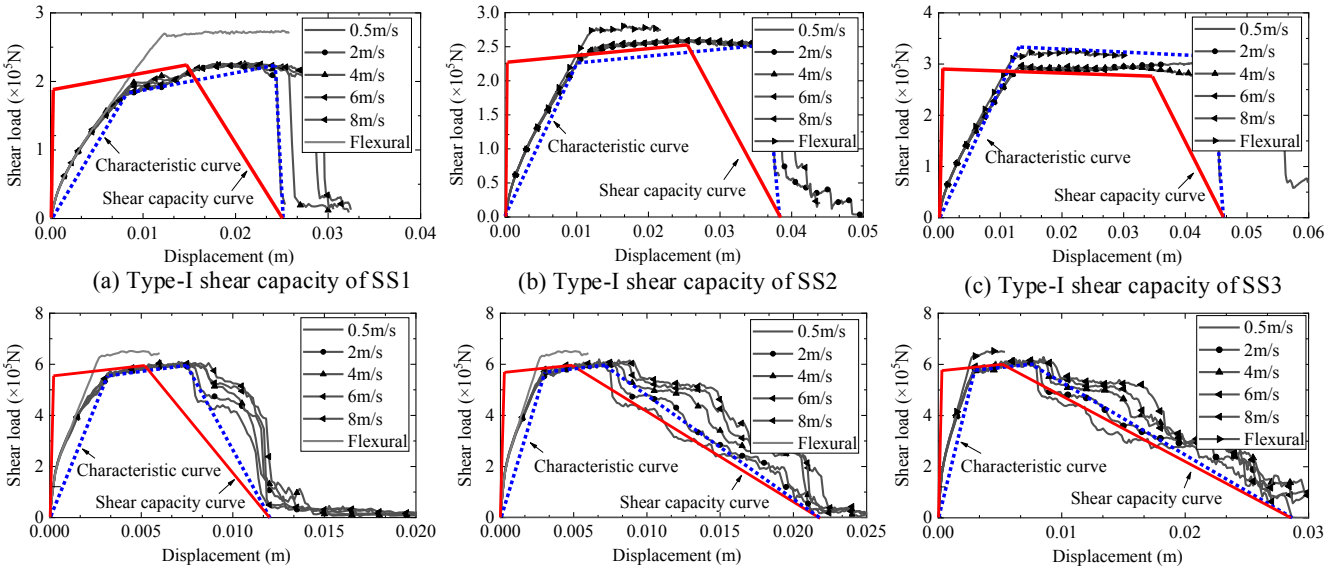

(a) Type-I shear capacity of SS1 (b) Type-I shear capacity of SS2 (c) Type-I shear capacity of SS3

(d) Type-II shear capacity of SS1 (e) Type-II shear capacity of SS2 (f) Type-II shear capacity of SS3

Fig. 20. Shear capacity curves of RC beams tested by Saatci et al. [8].

from the numerical simulation are in good agreement with the experimental data. For impact cases D-1300-5.56 and D-868-7.14, the numerically-obtained midspan displacements are somewhat smaller than the experimental data (Fig. 15(h) and (i)). Zhao et al. [23,45] developed detailed FE models with 3-D solid elements to simulate these impact events. As shown in Fig. 15, the results derived from the detailed FE models are consistent with the results obtained from the proposed models in this study. For impact cases D-1300-5.56 and D-868-7.14, the differences in midspan displacements between the numerical simulations and the experiments may be attributed to the uncertainty in material strengths (e.g., concrete) and the manufacturing errors (e.g., the position of the longitudinal reinforcement) [23,45]. Generally, the prediction accuracies of the midspan displacement and impact force results are acceptable for the D-beam series because the maximum error is less than 15%. For Series C-beam with shear failures, the predicted duration of the impact force was shorter than the experimental result, while the midspan displacements were larger than the measured values, indicating that the impacted beams were completely damaged without any more resistance. These differences are attributed to the fact that shear resistances were conservatively estimated, particularly the residual capacities after failures.

Fig. 16 presents the characteristic curve of shear resistance of RC members that Krauthammer et al. [52] recommended. Residual shear resistances after strength softening are considered in the capacity curve before the maximum deformation is approached. The shear capacity curve obtained from the membrane model (e.g., Fig. 11) often does not have the portion of the residual shear resistance. However, the residual resistance might actually exist based on the experimental results [52]. To investigate the influence of residual shear resistance on impact-induced responses, impact cases C-1300-5.56 and C-868-7.14 were simulated again with various residual resistance ratios, which can be defined by

$$\alpha_I = R_{rI}/R_{sI} \quad \alpha_{II} = R_{rII}/R_{sII} \tag{15}$$

where α_I and α_{II} are the residual resistance ratos of Type-I and Type-II shear failures, respectively; R_{rI} and R_{rII} are the residual strengths of Type-I and Type-II shear failures, respectively; R_{sI} and R_{sII} are the peak strengths of Type-I and Type-II shear failures, respectively.

As shown in Fig. 15(e), (f), (k) and (l), better agreements were obtained between the numerical and experimental data of the impact forces and the midspan displacements after including the residual shear resistances, particularly when the residual resistances are equal to 0.3–0.4 time the peak shear strength. Also, Fig. 14(f) indicates that the numerically-obtained failure pattern with both two shear cracks instead of only punching shear failure is more consistent with the experimental observation when α_I and α_{II}=0.3–0.4 for impact case C-868-7.14.

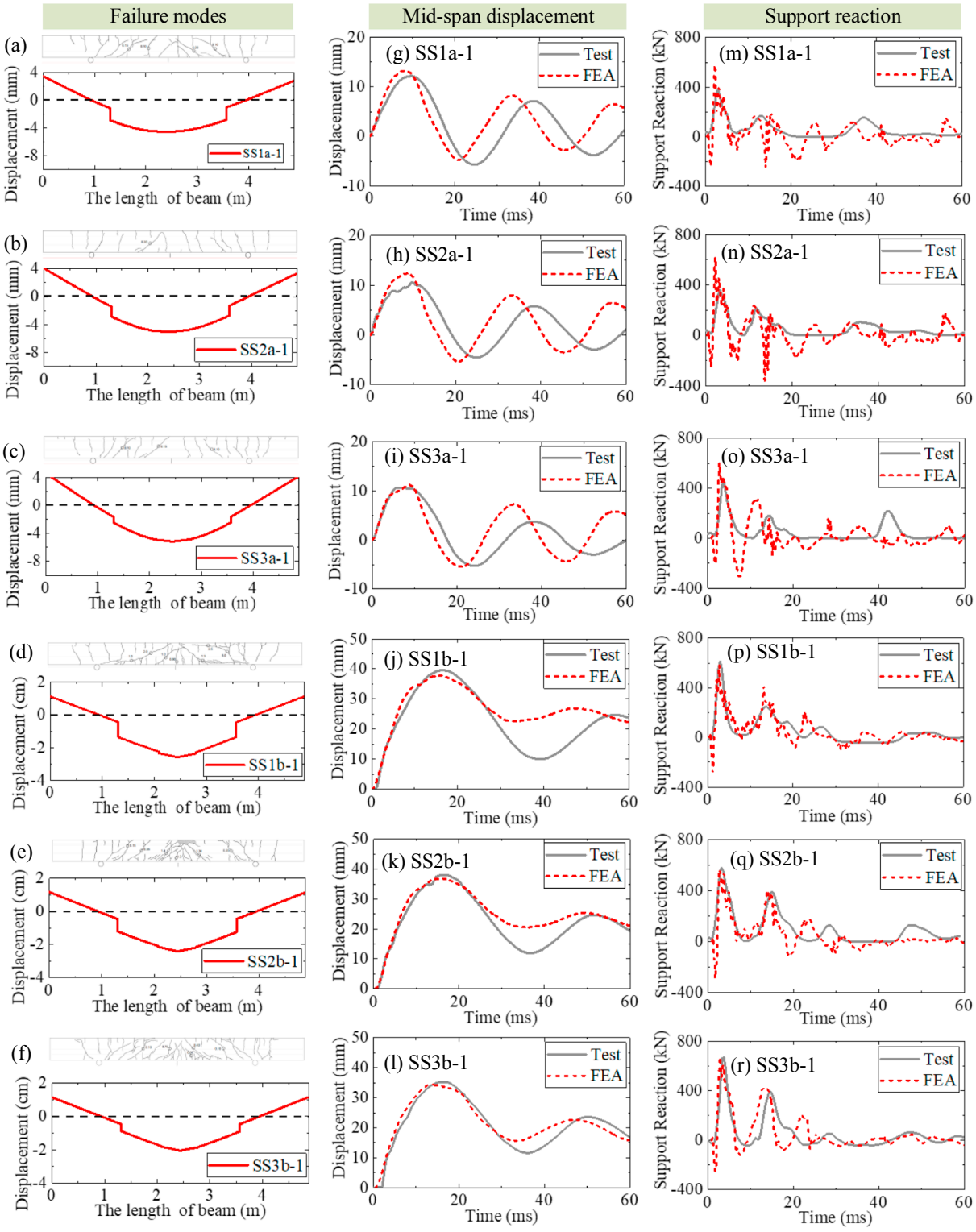

Fig. 21. Comparisons of impact responses between the experiments [8] and the FE simulations.

3.4.2. Impact tests on RC beams conducted by Xu and Zeng [51]

To further validate the proposed modeling method, the impact tests on the RC beams conducted by Xu and Zeng [51] were simulated. The test setup and the details and dimensions of the specimens are presented in Fig. 17(a) and (b), respectively. All the specimens had the dimensions of 310 mm in depth, 150 mm in width and 2700 mm in length. For each specimen, the longitudinal and transverse reinforcement ratios were 1.45% and 0.22%, respectively. The uniaxial compressive strength of the used concrete material was 26.9 MPa. All specimens were doubly reinforced with a total of six 16-mm diameter longitudinal reinforcement bars placed symmetrically. A 25 mm clear cover was used between the bars and the top and the bottom beam surfaces. Table 1 lists the material properties of the concrete and reinforcing steel bars in the specimens and impact mass and velocities for each impact case. More details on their impact tests can be found in Xu and Zeng [51]. Fig. 17 (c) and (d) illustrate the developed model with

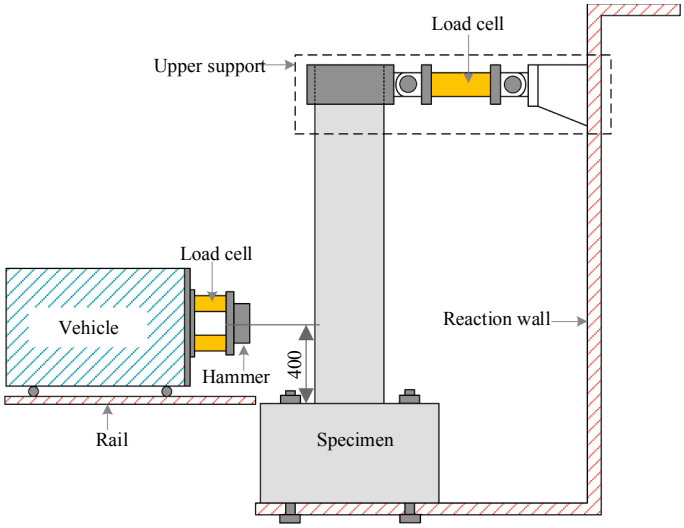

(a) Impact test setup of RC column (Demartino et al. 2017)

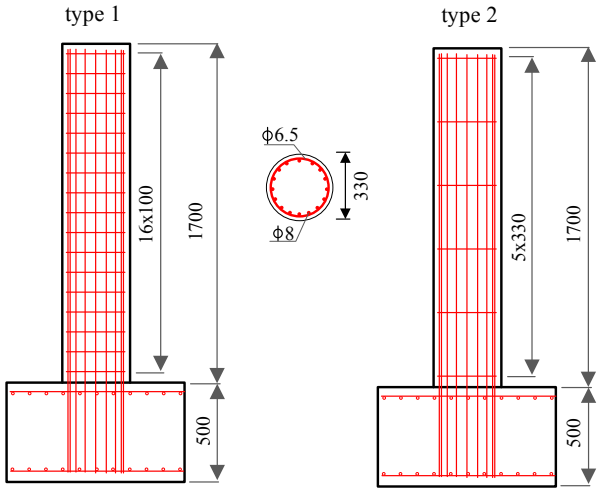

(b) Schematic of the RC column specimens (Unit: mm)

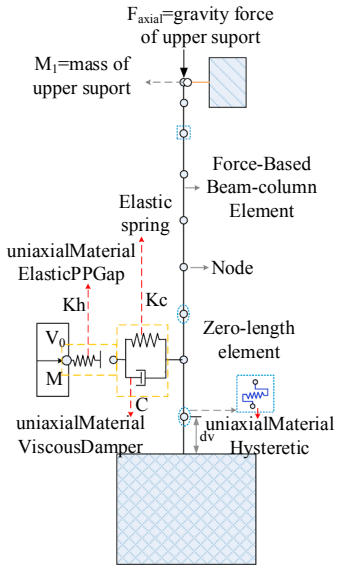

(c) Proposed model (Demartino et al. 2017)

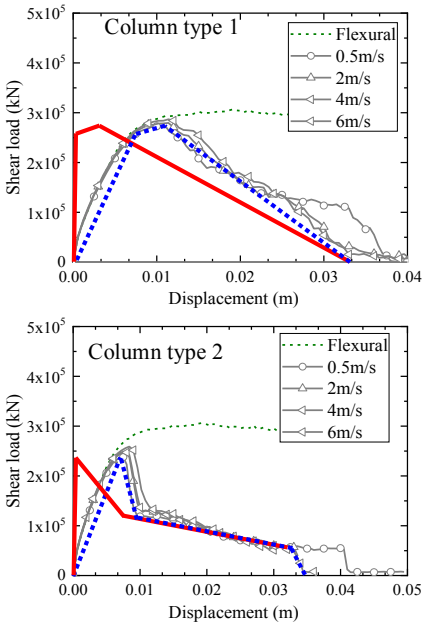

(e) Shear capacity (Type-I) of the RC column specimens.

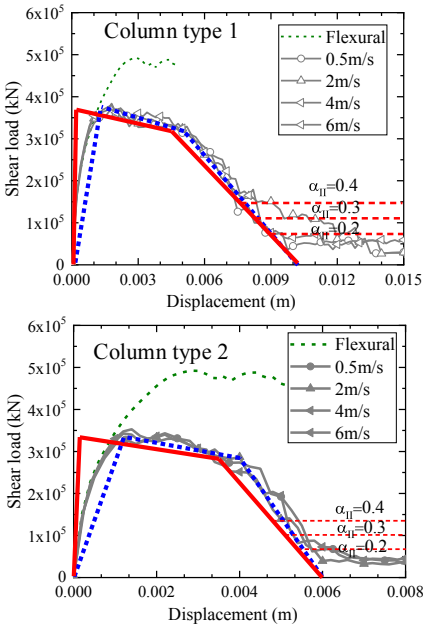

(d)Shear capacity (Type-II) of the RC column specimens.

Fig. 22. Impact tests on RC columns conducted by Demartino et al. [9] and the corresponding FE model.

fiber-based nonlinear beam-column elements. Similarly, model parameters (e.g., $K_c = 5.50 \times 10^8$ N/m and $C_L = 6.99$) were determined based on the approach mentioned above. Also, the shear capacity curves were obtained by the VecTor2 model and the suggested treatments to define the shear springs in the FE model, as shown in Fig. 17(e) and (f).

The predicted results are presented in Fig. 18 with the experimental data for comparisons. Generally, not only the impact-induced deformed pattern but also the impact forces and midspan deflections predicted using the proposed method are in good agreement with the measured results. In addition to the overall deformations, the punching shear (Type-II) cracks observed in the tested specimens BD2 to BD5 (particularly in the specimen BD3), and the Type-I shear cracks found in the specimen BD1 can be well captured by the proposed method (Fig. 18(a)–(e)).

3.4.3. *Impact tests on RC beams conducted by Saatci and Vecchio [8]*

Saatci and Vecchio [8] also performed the drop-hammer impact tests (Fig. 19) to examine the shear mechanism of reinforced concrete beams under impact loading. Two different impact energies (Table 1) and three transverse reinforcement ratios (ρ_T=0.1%, 0.2%, and 0.3%)were experimentally investigated. All the specimens had the cross-sectional dimensions of 410 mm in depth and 250 mm in width, the clear span of 3000 mm, and the longitudinal reinforcement ratio of 2.75%. Like the above tests, all specimens were doubly reinforced with the longitudinal bars (No. 30 bars in CSA Standard G30.18 with a 700 mm^2 cross-sectional area and a 29.9 mm nominal diameter) placed symmetrically. The thickness of concrete cover was 38 mm. Other details of the specimens are shown in Fig. 19. Table 1 lists the properties of the concrete and reinforcing steel bars. Similarly, the proposed fiber-based nonlinear beam-column models were developed with the shear springs modeled by the capacity curves

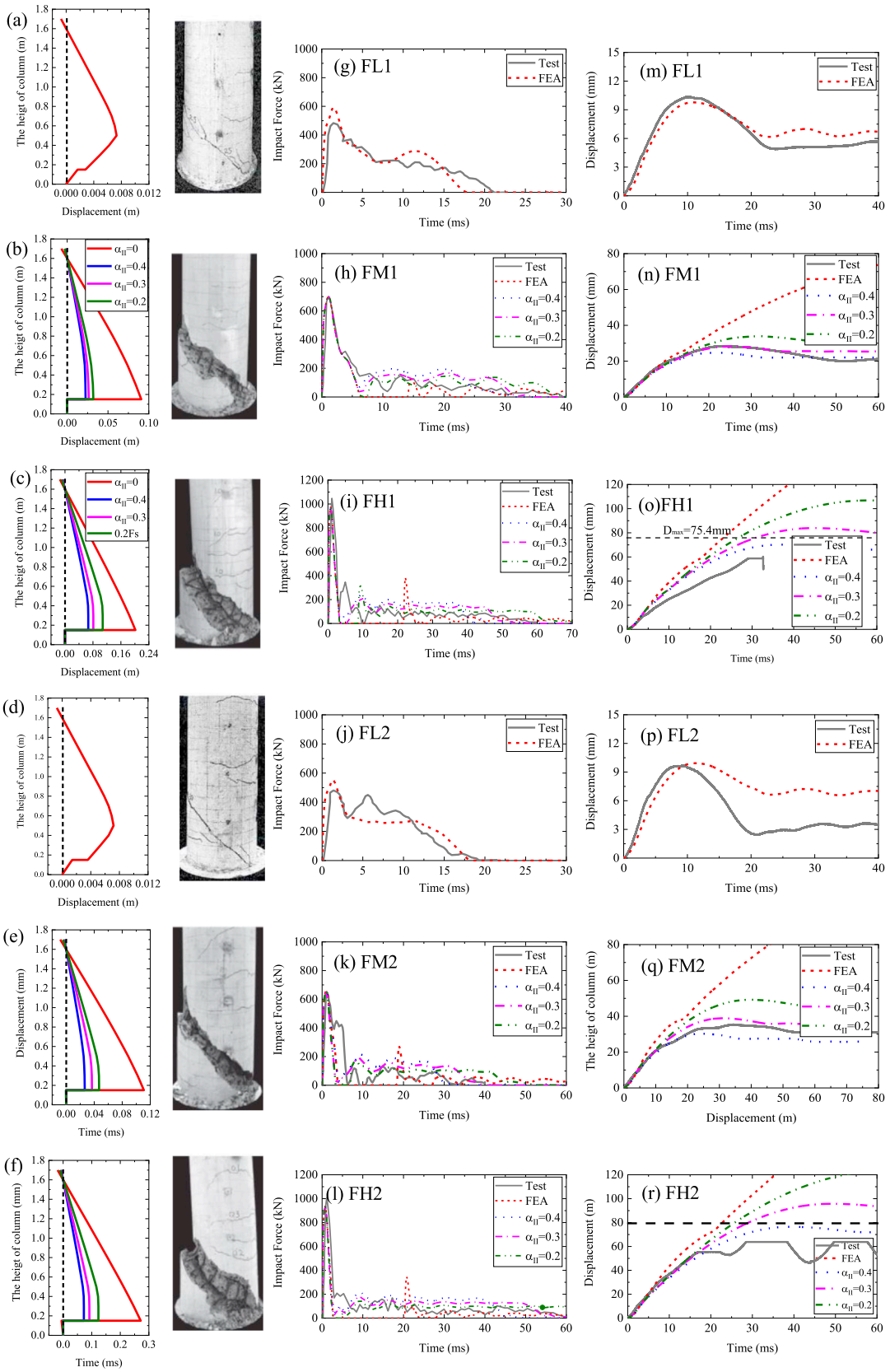

Fig. 23. Comparisons of impact responses between the experiments [9] and the FE simulations.

presented in Fig. 20. The corresponding numerical results are shown in Fig. 21. As well, the impact responses obtained from the proposed model are consistent with the experimental data. It is worth noting that there were no impact forces reported in Saatci and Vecchio [8], but the support reaction forces were measured in the tests. Hence, only the support reaction forces were compared, as shown in Fig. 21(m)–(r). Generally, the predicted

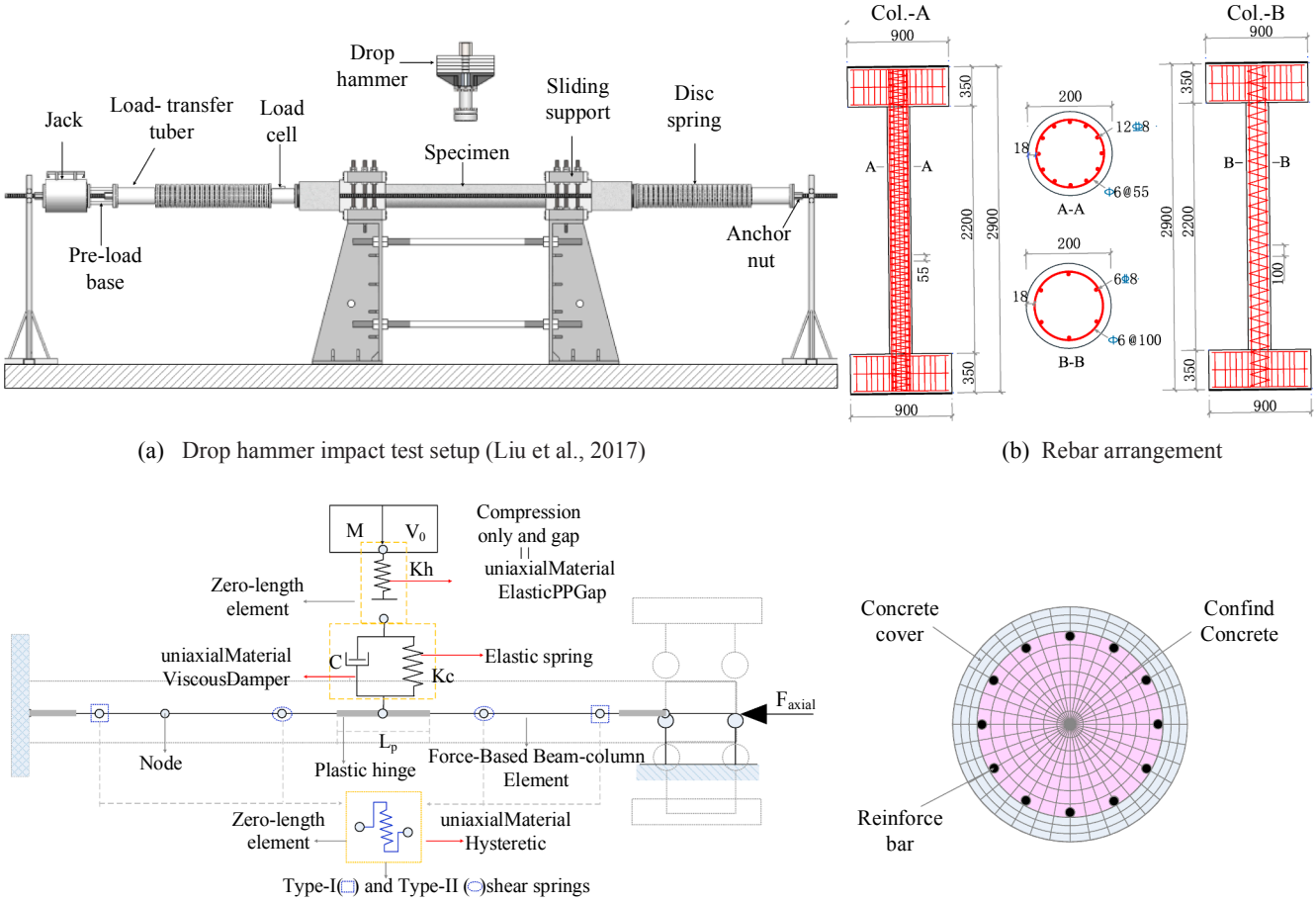

(a) Drop hammer impact test setup (Liu et al., 2017)

(b) Rebar arrangement

(c) Proposed model for impact simulation of axially-loaded RC columns

(d) Fiber section of beam element

Fig. 24. Impact tests on axially-loaded RC columns conducted by Liu et al. [7] and the proposed model.

reaction forces agreed with those measured from the experiments. It should be mentioned that because pressure sensors were used to measure the reaction forces, the tensile forces were omitted in the experimental results.

4. Modeling of RC columns and validations

RC columns are the critical load-carrying elements to support vertical loads in bridge and building structures. In addition to service loads, RC columns may be at higher risk for lateral impact loading (e.g., vessel and vehicle collisions) compared with beam members without axial loads. Thus, the need is evident to examine the applicability of the proposed modeling method for the impact simulations of axially-loaded RC columns under impact loading.

4.1. Horiziontal impact tests on RC columns conducted by Demartino et al. [9]

In addition to the impact tests on RC beams, the impact tests on circular RC columns were carried out by Demartino et al. [9]. Different from the above tests, the horizontal test setup was employed in the tests, as shown in Fig. 22(a). The horizontal collision facility consisted of an external drive mechanism and a test truck made of a four-wheeled hoper moving on a horizontal rail. An instrumented hammer, which had an 80 mm thick steel plate with a size of 580 mm long and 200 mm wide, was placed in the front of the test truck. The material properties of the specimens are summarized in Table 1. Parameters varied in the tests included: three impact energies (see Table 1) and two different transverse reinforcement ratios (ρ_T = 0.3% and 0.09%). The longitudinal reinforcement ratio was 0.9% for all the specimens. The column specimens had a diameter of 300 mm, a length of 1700 mm, and a clear height of 1600 mm, as shown in Fig. 22(b). The uniaxial compressive strength of the used concrete was 28 MPa, and the yielding strengths of the longitudinal and transverse reinforcements were 427 MPa and 416 MPa, respectively. Like the above treatments, the fiber-based nonlinear beam-column model (Fig. 22(c)) was developed. The shear capacity curves presented in Fig. 22(d) and (e) were used in the definition of the shear springs.

Fig. 23 presents the predicted force and displacement responses and the deformation patterns after the impacts along with the experimental data. For the failure modes, numerical simulations indicate that all the columns exhibit shear-dominated failures, which are consistent with the experimental results. For impact cases FL1 and FL2 with relatively slight shear damage, the predicted impact forces and displacements are in reasonable agreement with the experimental data, as shown in Fig. 23(g), (m), (j) and (h). For the other four impact cases with relatively large shear damage, the predicted duration of the impact force was shorter and the peak midspan displacements were larger in comparison with the experimental data. These are the same as those observed in Series C-beam of Zhao et al. [23,45]. Similarly, this is attributed to the fact that residual shear resistances more or less exist in reality. Thus, the influence of residual strength ratios (i.e., 0.2R_s to 0.4 R_s) was investigated, as shown in Fig. 23. Similar to Series C-beam of Zhao et al. [23], better agreements were achieved when 0.3–0.4R_s was considered. Axial preloads were omitted in the tests. However, vehicle

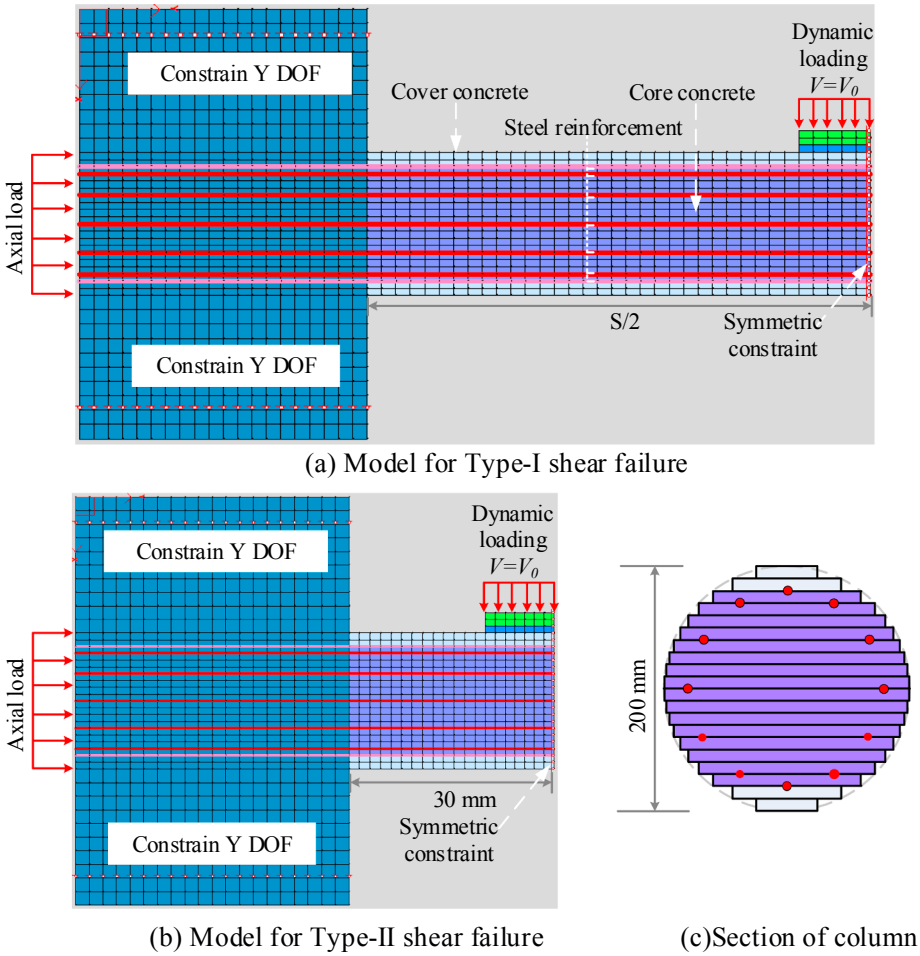

Fig. 25. VecTor2 model for predicting column shear resistances.

impacts are usually regarded as low-elevation (unsymmetrical) impacts (Gurbuz et al. [53]) on axially-loaded RC columns. If sufficient experimental data of axially-loaded RC columns under low-elevation impacts become available in the future, the proposed modeling method should be further validated.

4.2. Impact tests on axially-loaded RC columns conducted by Liu et al. [7]

Compared with the impact tests on RC beams, few experiments had been performed to investigate the impact behaviors of axially-loaded RC columns. Liu et al. [7] recently carried out such tests to explore the impact-resistant behaviors of axially-loaded RC columns. The experimental results were employed here to validate the proposed modeling method. In addition to the eight specimens given in [7], four more specimens were tested separately to investigate the influence of column aspect ratio on the impact responses [4]. A total of 12 impact scenarios were simulated in this study. As illustrated in Fig. 24(a), axial loads were applied simultaneously during lateral impact testing. Primary varied parameters included axial load ratio (0%, 14% and 28%), impact energy (low and high), reinforcement ratio (ρ_L = 1.92%, ρ_T = 1.3% and ρ_L = 0.96%, ρ_T = 0.72%) and column aspect ratio (1/7, 1/6 and 1/5). Different failure modes with various damage extents were observed in the impact tests. Two different arrangements of the longitudinal and transverse reinforcements are shown in Fig. 24(b). Additional details on the impact tests on the axially-loaded RC columns can be found in [4,7].

Using the proposed modeling method, the FE models shown in Fig. 24(c) and (d) were developed to analyze the impact behaviors of axially-loaded RC columns. In addition to the contact-impact point, plastic hinges were defined at the two ends of the columns in the FE models. The axial loads were applied at one of the column ends. Similarly, the membrane models with VecTor2 (Fig. 25) were created to estimate the shear capacity curves (Fig. 26) for two types of shear cracks.

The FE results of the columns are presented in Figs. 27–29 along with corresponding experimental data. Good agreements were achieved between the experimental and numerical results, indicating that the proposed modeling method is also applicable to the impact analysis of axially-loaded RC columns. For impact cases E2F3L6 and E2F3S2, the collapses of the column specimens can be fully captured by the proposed method. Also, the shear damages or failures of the column specimens in the cases E2F3S1 and E2F3S2 were predicted. Certainly, unlike the numerical simulations, shear failure patterns observed from the experiments were not symmetrical because the material properties were somewhat random for concrete. It can be concluded that the proposed method is capable of identifying the failure modes (e.g., flexural and shear failure) of the axially-loaded RC columns under impact loading.

5. Summary of the proposed method and discussions

To clearly describe the procedure of the proposed modeling method, a general procedure is summarized in the section. Meanwhile, some modeling issues (e.g., mesh sensitivity) are discussed for the general modeling procedure, and comparisons between the proposed method and the exsiting method are presented.

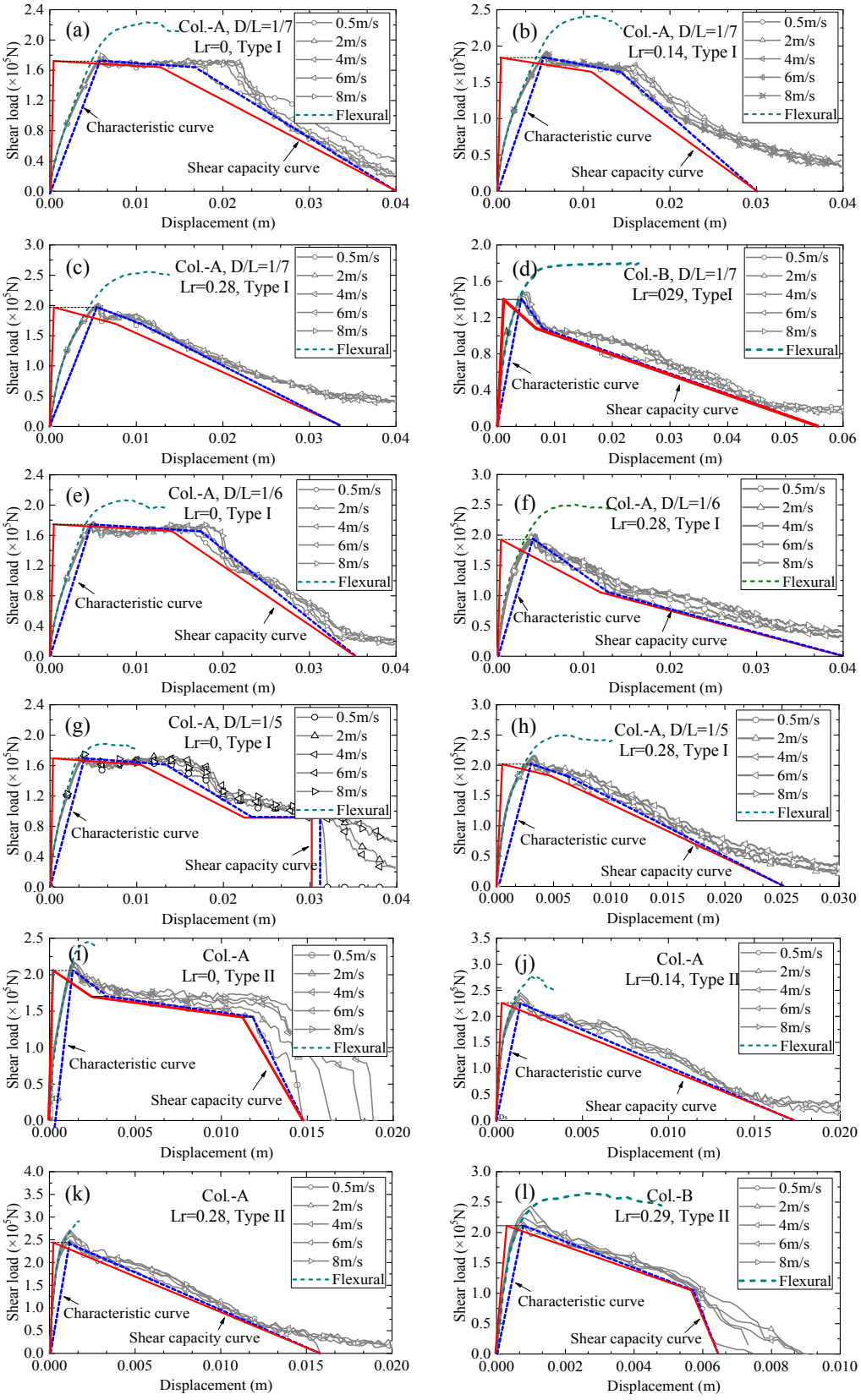

Fig. 26. Shear capacity curves of axially-loaded columns obtained from VecTor2.

5.1. General procedure of the proposed modeling method

Based on all the above investigations, the proposed modeling procedure for evaluating impact behaviors of RC beams and columns can be summarized as

Step I. Determining the material properties of concrete and reinforcing steel with strain-rate effects. The uniaxial Propovics

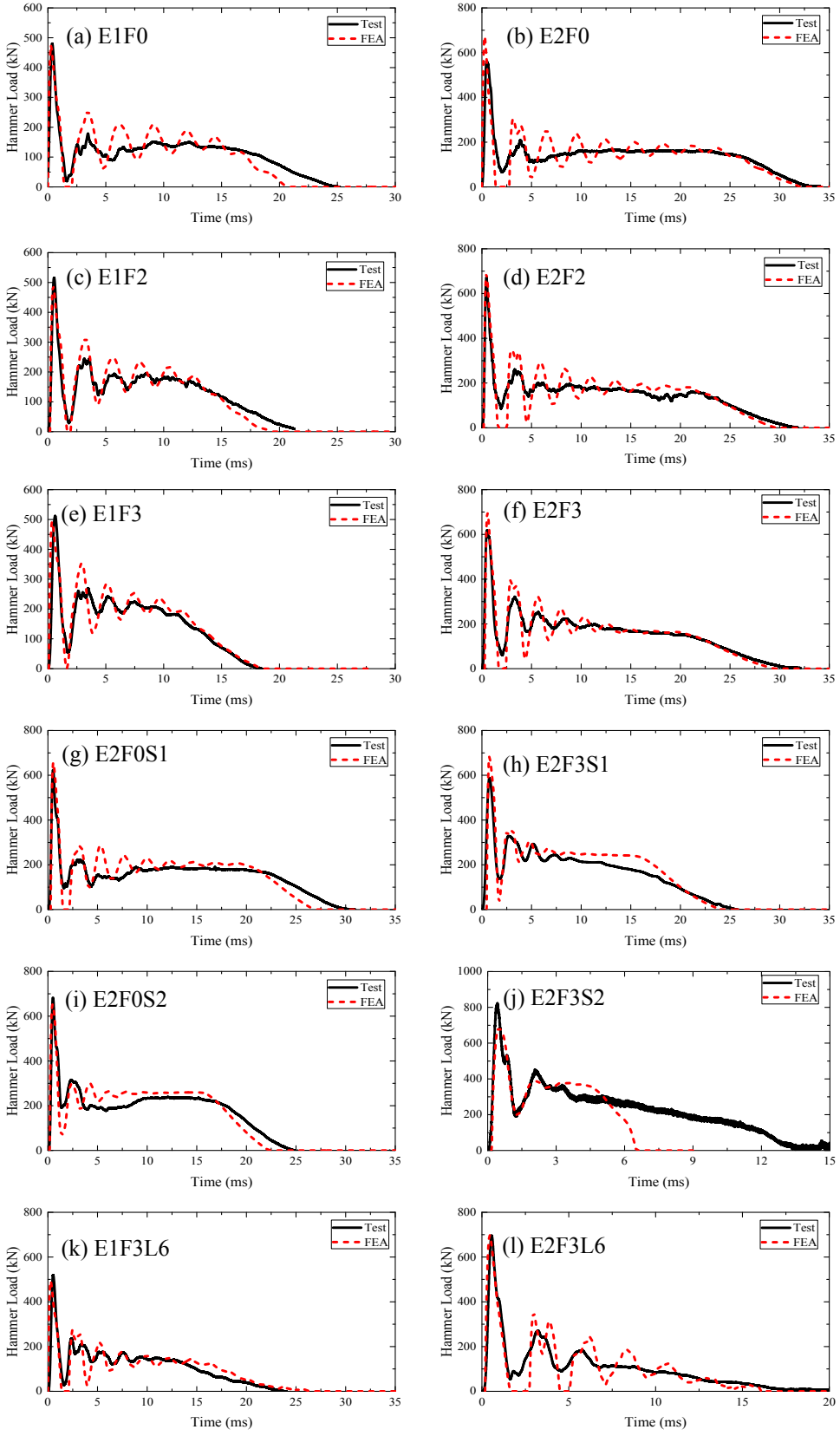

Fig. 27. Comparisons of impact forces between the experiments [7] and the FE simulations.

material model (Concrete04) and the Giuffre-Menegotto-Pinto model (Steel02) in OpenSees can be used for concrete and reinforcing steel bars, respectively. Eqs. (3)–(11) can be used to consider strain-rate effects.

Step II. Obtaining shear capacity curves for two types of shear failures. The MCFT-based FE code VecTor2 can be used to obtain shear spring curves. More details about how to obtain shear capacity curves can found in Section 3.2.

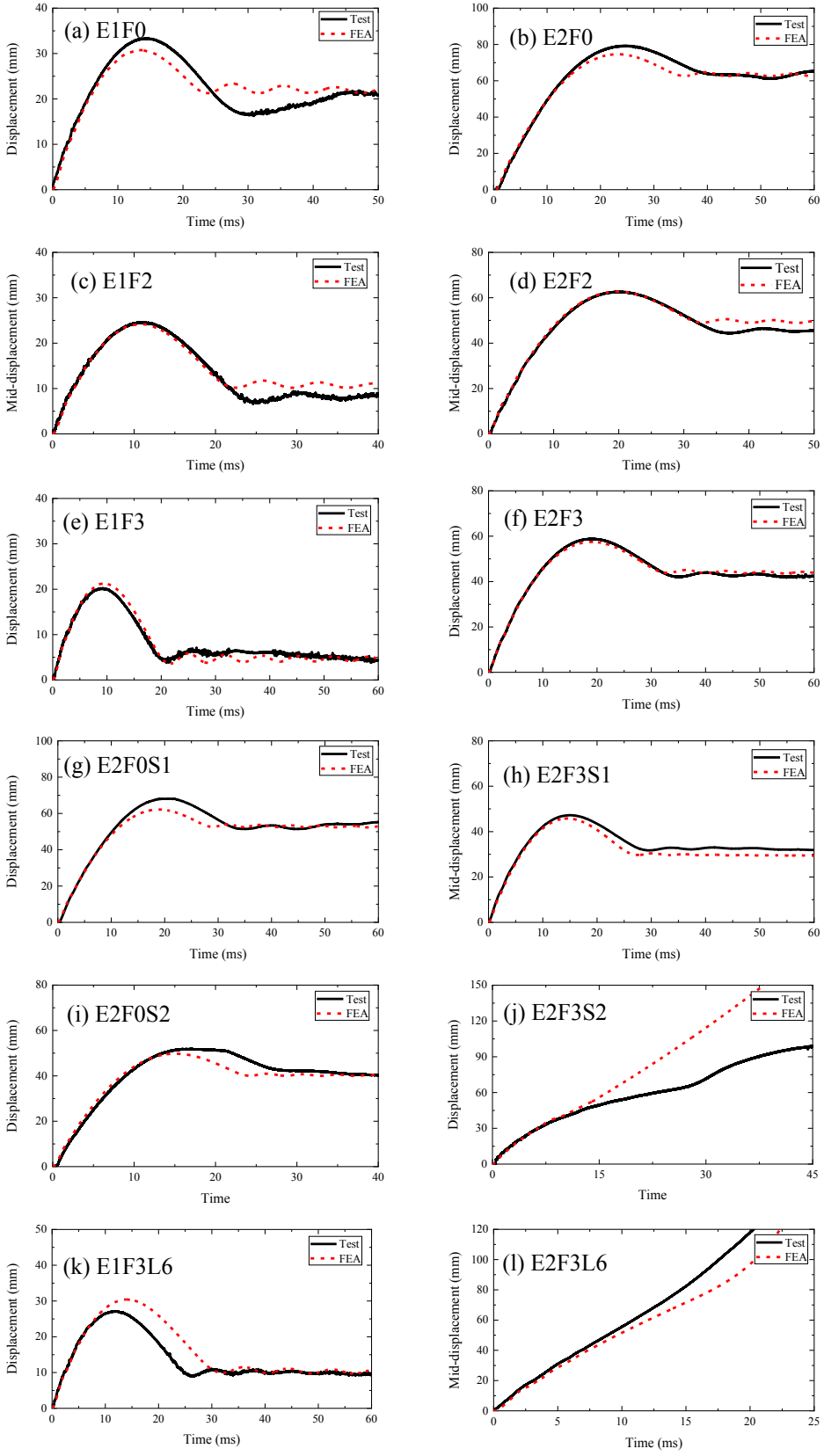

Fig. 28. Comparisons of midspan deflections between the experiments [7] and the FE simulations.

Step III. Creating nonlinear beam-columns elements for modeling the impacted RC members or structures. The force-based elements with fiber-based cross sections in OpenSees can be used.

Step IV. Defining two types of shear springs in the FE model of the impacted RC members. The detailed procedure of defining shear springs can be found in the end of Section 3.3.

Step V. Modeling impacting objects. For rigid impact tests, a lumped mass element and an elastic spring element can be used to

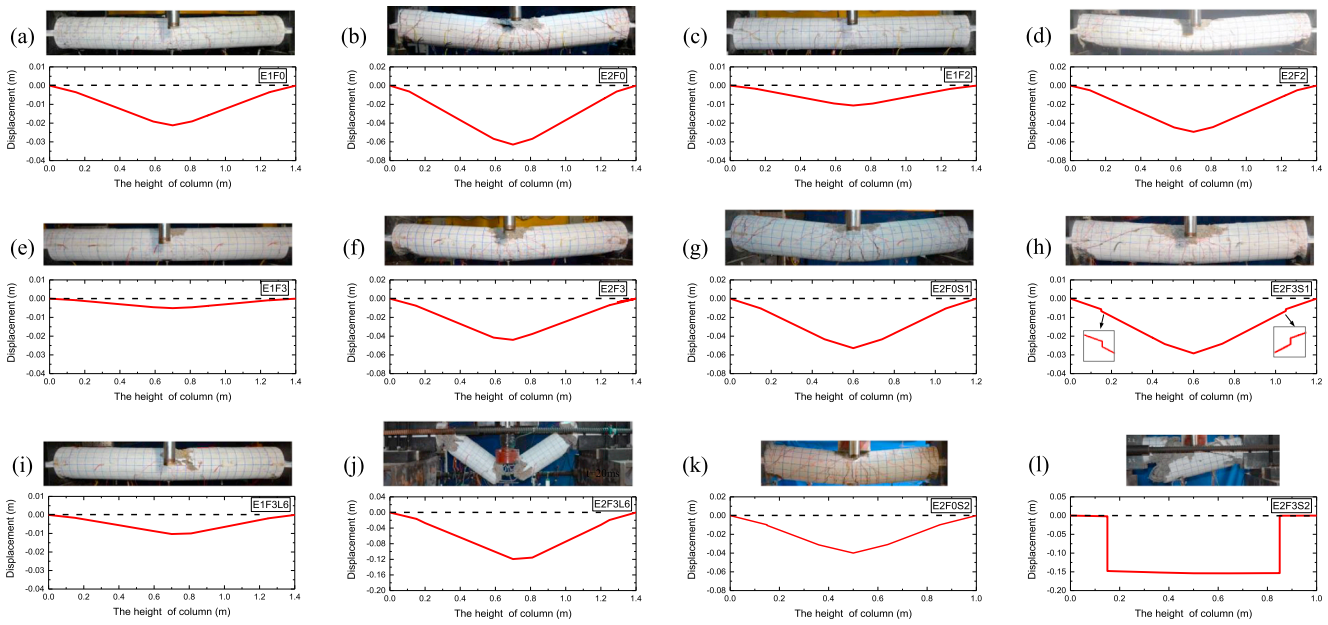

Fig. 29. Comparisons of failure modes between the experiments [7] and the FE simulations.

model the mass (M_h)and stiffness (K_h) of a rigid hammer, respectively. Since hammers are often much more rigid than the impacted member, K_h can be set to be 1×10^9 N/m.

Step VI. Modeling interactions between the impacting object and the impacted member or structure using macroelements. In OpenSees, the uniaxial materials *contact-spring* (Fig. 2(b)) and *linear-viscous-damper* (Fig. 2(c)) can be used to consider the contact stiffness and damping, respectively. Sometimes, the nonlinear contact model can be considered to represent the local damage around contact-impact zones (e.g., S1322 and S2222 in Fujikake et al. [6]). Further studies should be conducted to develop the nonlinear contact model.

Step VII. Applying initial impact velocity. In explicit dynamic FE code (e.g., LS-DYNA), the initial impact velocity of the impacting object can be directly defined. In the FE code with an implicit solver (e.g., OpenSees), the initial impact velocity can be obtained by exerting an instant load (or impulse) in accordance with Eqs. (1) and (2).

The flexural-critical RC beams mentioned in Section 2 were simulated again by using the above general modeling procedure. Different from the analyses in Section 2, the FE models included shear springs. This means that the impact the failure modes of the RC beams were treated as unknown. It can be observed from Figs. 5–7 that the models with shear springs yield the same results as those without shear springs. Table 3 summarizes that the predicted and measured peak impact force and maximum displacements as well as the ratios of experimental to predicted impact responses for all impact cases mentioned above. It can be found that the average value of the experimental to predicted peak impact force ratio is 0.988 and the coefficient of variation (COV) is 1.27%. For the maximum displacements, the average value of the experimental to predicted response ratio is 0.97, and the COV is 0.8%. Overall, the applicability of the proposed modeling method was widely validated for the low-velocity impact simulations of RC beams and columns.

5.2. Discussions about mesh size and strain-rate parameter

The mesh sensitivity should be discussed for the modeling method summarized above. Impact cases S1616-0.6 in [6] and D-1700-4.6 in [45] were used to discuss the mesh sensitivity of flexural- and shear-critical RC members, respectively. As shown in Fig. 30, at least eight elements are required for modeling RC members due to the presence of shear springs. Two refined mesh schemes were employed to investigate the mesh sensitivity (Fig. 30). Numerical results (Fig. 31) indicate that all three different meshes yield the same results. Hence, only eight elements shown in Fig. 30 are needed for the proposed modeling method. This implies that the proposed modeling method is robust in terms of selecting the number of elements. As mentioned above, a plastic hinge with the length equal to the height of the member's cross-section [29] needs to be specified at the contact-impact zone. Hence, only one element should be arranged between the punching shear springs and the contact-impact point because of the presence of the plastic hinge and the punching shear springs.

On the other hand, the average impact velocity was employed in the proposed modeling method to approximately consider the strain-rate effects and estimate the dynamic increase factors. The influence of this assumption should be evaluated. As shown in Fig. 32, three impact cases with relatively high velocities and various failure modes were used to examine the influence of this assumption. Three different velocities (i.e., $0.25V_0$, $0.5V_0$ and V_0) were used to estimate the DIFs of concrete and reinforcing bars. It can be observed from Fig. 32 that the impact responses are not sensitive to the selection of impact velocity for the determination of the DIFs. As mentioned above, this is because the relationship between the strain rate and the dynamic increase factor is usually logarithmic (e.g., Eqs. (3) and (4)). The strain rate of the static or quasi-static loading is usually 1×10^{-5} or 10^{-4}, whereas the strain rate in low-velocity impacts ($\sim 10^0$ or 10^1) is many orders of magnitude higher than that of the static or quasi-static cases. Therefore, it is essential to include strain-rate effects in impact simulations. But, the impact responses are not sensitive to the selection of impact velocity when it changes in a limited range compared with the difference between the impact loading and the static loading. Based on the above observations, the assumption of using average impact velocity is acceptable.

5.3. Comparisons between the proposed model and the detailed FE model

Impact cases S1616-1.2 in [6] and E1F2 in [7] were employed to compare the computational efficiency between the proposed model and the detailed FE model with 3-D solid elements. Table 4 lists the calculation time and the size of the main output file for the proposed model

Table 3
Summary of experimental and numerical results.

Reference	NO.	ID	Impact force			Displacement		
			Test (kN)	Proposed model (kN)	Test/FEA	Test (mm)	Proposed model (mm)	Test/FEA
Fujikake et al. [6]	1	1322–0.3	177	178	1.006	7.79	6.02	0.773
	2	1322–0.6	258	249	0.965	11.73	11.14	0.950
	3	1322–1.2	310	353	1.139	22.89	21.24	0.928
	4	1322–2.4	340	427	1.256	27.86	30.67	1.101
	5	1616–0.15	121	123	1.017	6.22	5.53	0.889
	6	1616–0.3	168	173	1.030	11.16	9.64	0.864
	7	1616–0.6	245	248	1.012	19.43	18.49	0.952
	8	1616–1.2	312	348	1.115	36.9	35.3	0.957
	9	2222–0.3	199	180	0.905	7.79	5.67	0.728
	10	2222–0.6	263	254	0.966	11	10.7	0.973
	11	2222–1.2	314	360	1.146	21.44	20.21	0.943
	12	2222–2.4	441	370	0.839	32.51	31.69	0.975
Zhao [45]	13	D-1700	1344	1173	0.873	41.22	40.43	0.981
	14	D-1300	1500	1389	0.926	49	42	0.857
	15	D-868	1647	1697	1.030	47.4	43.4	0.916
	16	C-1700	1377	1183	0.859	–	–	–
	17	C-1300	1471	1404	0.954	67	63.1	0.942
	18	C-868	1750	1706	0.975	67.8	66.4	0.979
Xu and Zeng [51]	19	BD1	891	670	0.752	11.9	10.8	0.908
	20	BD2	1396	1183	0.847	23.7	26.1	1.101
	21	BD3	1940	1898	0.978	64.9	69.5	1.071
	22	BD4	1466	1310	0.894	78.5	76.1	0.969
	23	BD5	980	860	0.878	36.5	34.7	0.951
Saatci et al. [8]	24	SS1a-1	–	1253	–	12.2	13.26	1.087
	25	SS2a-1	–	1252	–	10.54	12.37	1.174
	26	SS3a-1	1407	1260	0.896	10.7	11.2	1.047
	27	SS1b-1	1765	1580	0.895	39.5	37.78	0.956
	28	SS2b-1	1645	1580	0.960	38	36.9	0.971
	29	SS3b-1	–	1590	–	35.26	34.4	0.976
Demartino et al. [9]	30	FL1	483	581	1.203	10.3	9.77	0.949
	31	FL2	481	548	1.139	9.63	9.92	1.030
	32	FM1	702	704	1.003	28.3	27.7	0.979
	33	FM2	652.7	663	1.016	35.4	32.1	0.907
	34	FH1	1047	992.5	0.948	75.4	83.8	1.111
	35	FH2	1009	937.7	0.929	79.3	89.9	1.134
Liu et al. [7]	36	E1F0	480	472.6	0.985	33.3	30.5	0.916
	37	E2F0	563.2	671.8	1.193	79.2	74.4	0.939
	38	E1F2	515.3	486.9	0.945	24.5	24	0.980
	39	E2F2	671.7	687.3	1.023	62.5	62.5	1.000
	40	E1F3	511.7	492.7	0.963	20.3	21.1	1.039
Liu et al. [7]	41	E2F3	617.4	696	1.127	58.8	56.7	0.964
	42	E2F0S1	623.5	656.7	1.053	68	61.8	0.909
	43	E2F3S1	587	682	1.162	47.2	46	0.975
	44	E2F0S2	682.6	652	0.955	51.8	49.6	0.958
	45	E2F3S2	882.9	680	0.770	–	–	–
	46	E1F3L6	519	493	0.950	27.1	30.2	1.114
	47	E2F3L6	695.5	697	1.002	–	–	–
			Average		0.988	Average		0.970
			COV		0.0127	COV		0.008

and the detailed FE model. As shown in Table 4, the computational efficiency was significantly improved, and the memory size required was greatly reduced when using the proposed method. For these two cases, the increases in computational efficiency are ~340 times and ~1020 times, respectively. Detailed simulations often have to be run by the FE code (e.g., LS-DYNA) with explicit time integration because of the presence of the complex contact between impacting objects and RC members. For the explicit time integration, a particular treatment (e.g., dynamic relaxation) is required for exerting the preload and obtaining the stable initial state before impact loading. It is time-consuming and complicated in real-world impact problems (e.g., vessel/vehicle collision analysis) [2]. For the proposed method, the implicit solver (e.g., OpenSees) can be used to avoid the difficulty of applying the preload. Also, nonlinear beam-column elements instead of solid elements with reduced integration were adopted in the proposed method to model RC beams and columns. As a result of the change, the hourglass issue typically existed in detailed FE models with 3-D solid elements can be avoided in nature. Of course, compared with detailed FE models, additional macro-elements (e.g., shear springs) are required in the proposed model.

6. Conclusions

This study proposed a modeling method to efficiently predict both flexural and shear responses of RC beams and columns subjected to low-velocity impact loading. In the proposed FE model, a macroelement-based model was developed to describe the interaction between impacting objects and impacted RC members. Typical fiber-based nonlinear beam-column elements were employed to model the nonlinear responses, and a simple approach was developed to account for strain-rate effects of concrete and reinforcing steel. Shear springs were added to capture the two types of shear damages (i.e., normal and punching

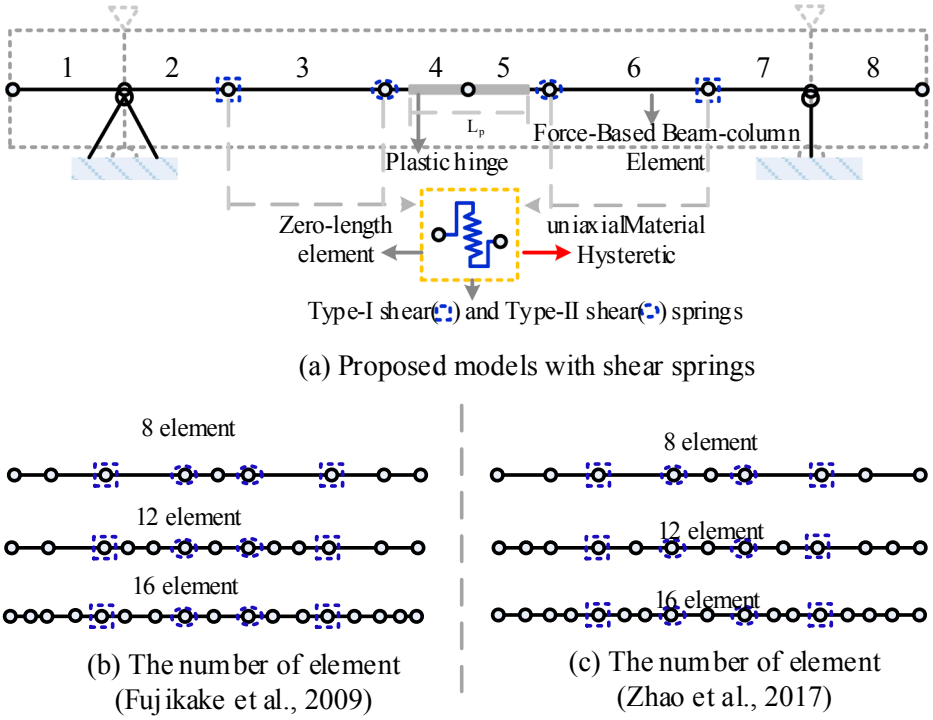

Fig. 30. Different mesh schemes for impact simulations.

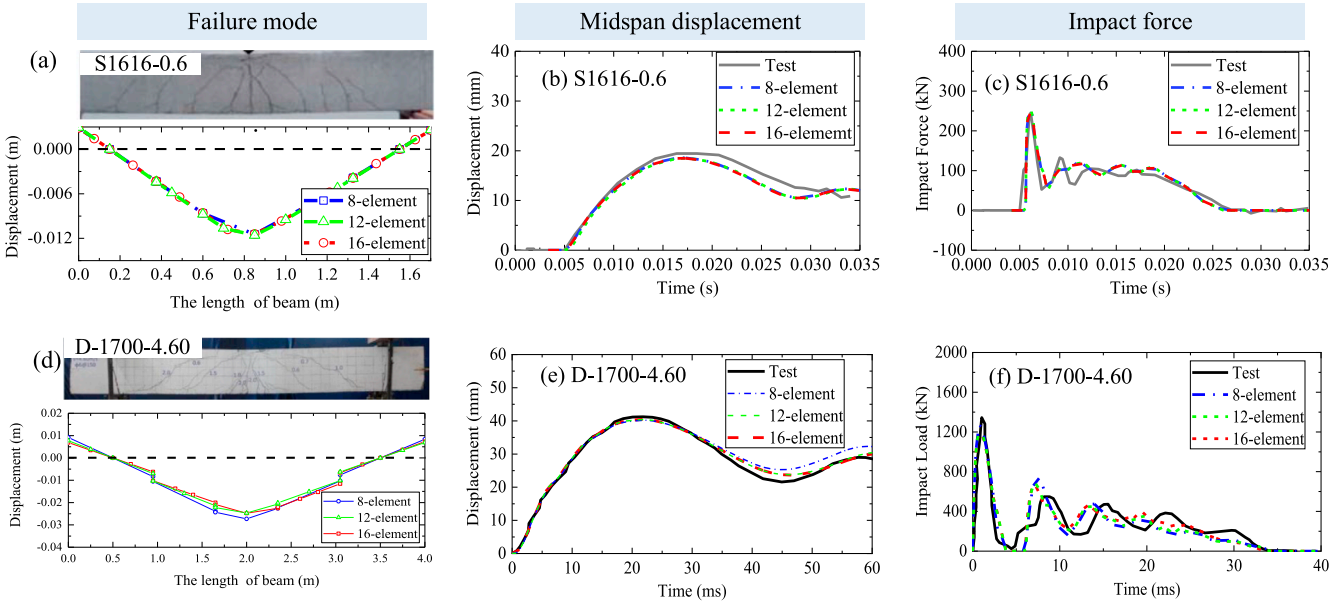

Fig. 31. Numerical results of mesh sensitivity.

shear cracks) due to impact loading. In addition, a simple procedure was presented to determine the shear capacity curves of the shear springs.

A total of 47 impact tests reported in references were collected and used to validate the proposed modeling method. The proposed method exhibited satisfactory performance on predicting the impact forces, the impact-induced deflections, and the failure modes of RC beams and columns. In addition, the proposed method is significantly superior to the detailed FE models with 3-D solid elements in computational efficiency (two or three orders of magnitude faster). Moreover, the proposed modeling can be readily applied without coding in any FE software that includes typical fiber-based nonlinear beam-column elements and discrete macro-elements. This advantage greatly facilitates the application of the proposed method in impact simulations of infrastructure such as bridge structures subjected to vessel and vehicle collisions.

Compared with low-velocity impacts, local damages (e.g., penetration and scabbing) around the contact-impact zone become much heavier in high-velocity impacts (e.g., aircraft impact and blast). Due to the differences between low-velocity impacts and high-velocity impacts, further studies need to be performed to extend the proposed modeling method for high-velocity impact analysis in the future.

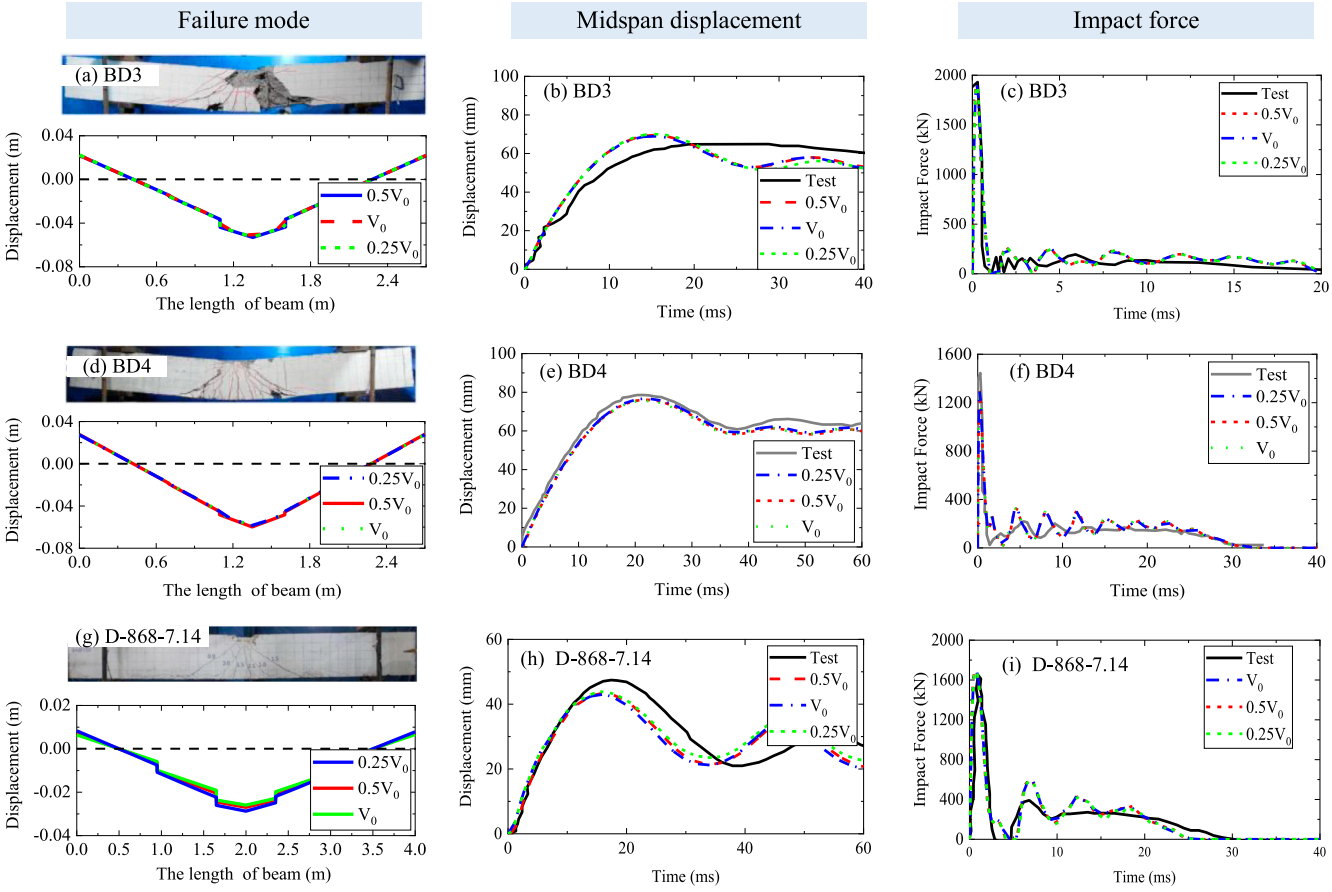

Fig. 32. Influence of the velocity on the equivalent DIF.

Table 4
Comparisons between the proposed model and the detailed FE models.

Mode Type	S1616-1.2 in [6]		E1F2 in [7]	
	Detailed model	Proposed model	Detailed model	Proposed model
Execution time	~23 min	4 sec	~12 h	41 sec
Output file size (MB)	563 MB	840 KB	6.2 GB	900 KB
Numerical integration	Only explicit	Implicit or explicit	Only explicit	Implicit or explicit
Macro-elements	Not required	Required	Not required	Required

Note. Data from the same computer with Intel(R) Core (TM) i7-4790 (CPU); and the detailed FE models of impact cases S1616-1.2 and E1F2 used can be found in Fan and Yuan [16] and Liu et al. [7], respectively.

Acknowledgments

This research is supported by the National Key Research and Development Program of China (Grant Number: 2018YFC0705405), the Major Program of Science and Technology of Hunan Province (Grant Number: 2017SK1010; 2016GK2025), and the National Natural Science Foundation of China (Grant Number: 51308202). The authors are very grateful to Prof. Frank Vecchio for his help regarding the use of the computer code VecTor2. The authors would also like to thank Mr. Jiguang Wu for the valuable assistance in retrieving experimental data.

Appendix A. Supplementary material

Supplementary data to this article can be found online at https://doi.org/10.1016/j.engstruct.2019.05.082.

References

[1] AASHTO. Guide Specifications and Commentary for Vessel Collision Design of Highway Bridges, 2nd ed. Washington, D.C.; 2009.
[2] Fan W, Xu X, Zhang Z, Shao X. Performance and sensitivity analysis of UHPFRC-strengthened bridge columns subjected to vehicle collisions. Eng Struct 2018;173:251–68.
[3] Buth CE, Williams WF, Brackin MS, Lord D, Geedipally SR, Abu-Odeh AY. Analysis of large truck collisions with bridge piers: phase 1, report of guidelines for designing bridge piers and abutments for vehicle collisions. College Station, Texas: Texas Transportation Institute, Texas A & M University System; 2010.
[4] Fan W, Liu B, Consolazio G. Residual capacity of axially-loaded circular RC columns after lateral low-velocity impact. J Struct Eng 2019;145.
[5] Adhikary SD, Li B, Fujikake K. State-of-the-art review on low-velocity impact response of reinforced concrete beams. Mag Concr Res 2016;68:701–23.
[6] Fujikake K, Li B, Soeun S. Impact response of reinforced concrete beam and its analytical evaluation. J Struct Eng 2009;135:938–50.
[7] Liu B, Fan W, Guo W, Chen B, Liu R. Experimental investigation and improved FE

modeling of axially-loaded circular RC columns under lateral impact loading. Eng Struct 2017;152:619–42.
[8] Saatci S, Vecchio FJ. Effects of shear mechanisms on impact behavior of reinforced concrete beams. ACI Struct J 2009;106:78.
[9] Demartino C, Wu JG, Xiao Y. Response of shear-deficient reinforced circular RC columns under lateral impact loading. Int J Impact Eng 2017;109:196–213.
[10] Sha Y, Hao H. Laboratory tests and numerical simulations of barge impact on circular reinforced concrete piers. Eng Struct 2013;46:593–605.
[11] Chen L, Xiao Y, El-Tawil S. Impact tests of model RC columns by an equivalent truck frame. J Struct Eng 2016;142:04016002.
[12] Consolazio GR, Cowan DR. Nonlinear analysis of barge crush behavior and its relationship to impact resistant bridge design. Comput Struct 2003;81:547–57.
[13] Do TV, Pham TM, Hao H. Dynamic responses and failure modes of bridge columns under vehicle collision. Eng Struct 2018;156:243–59.
[14] Thilakarathna HMI, Thambiratnam DP, Dhanasekar M, Perera N. Numerical simulation of axially loaded concrete columns under transverse impact and vulnerability assessment. Int J Impact Eng 2010;37:1100–12.
[15] Yuan P, Harik IE. Equivalent barge and flotilla impact forces on bridge piers. J Bridge Eng 2010;15:523–32.
[16] Fan W, Yuan WC. Numerical simulation and analytical modeling of pile-supported structures subjected to ship collisions including soil–structure interaction. Ocean Eng 2014;91:11–27.
[17] Abdelkarim OI, ElGawady MA. Performance of bridge piers under vehicle collision. Eng Struct 2017;140:337–52.
[18] Consolazio GR, Cowan DR. Numerically efficient dynamic analysis of barge collisions with bridge piers. J Struct Eng 2005;131:1256–66.
[19] Fan W, Yuan WC, Yang Z, Fan QW. Dynamic demand of bridge structure subjected to vessel impact using simplified interaction model. J Bridge Eng 2011;16:117–26.
[20] Fan W, Yuan WC, Zhou M. A nonlinear dynamic macro-element for demand assessment of bridge substructures subjected to ship collision. J Zhejiang Univ-Sci A 2011;12:826–36.
[21] Guner S. Performance assessment of shear-critical reinforced concrete plane frames. Ann Arbor: University of Toronto (Canada); 2008. p. 464.
[22] Guner S, Vecchio FJ. Simplified method for nonlinear dynamic analysis of shear-critical frames. ACI Struct J 2012;109:727–37.
[23] Zhao D-B, Yi W-J, Kunnath SK. Numerical simulation and shear resistance of reinforced concrete beams under impact. Eng Struct 2018;166:387–401.
[24] Bertrand D, Kassem F, Delhomme F, Limam A. Reliability analysis of an RC member impacted by a rockfall using a nonlinear SDOF model. Eng Struct 2015;89:93–102.
[25] Consolazio GR, Davidson MT. Simplified dynamic analysis of barge collision for bridge design. Transp Res Rec 2008:13–25.
[26] Fan W, Liu YZ, Liu B, Guo W. Dynamic ship-impact load on bridge structures emphasizing shock spectrum approximation. J Bridge Eng 2016;21:04016057.
[27] Mazzoni S, McKenna F, Scott MH, Fenves GL. OpenSees command language manual. Berkeley, Calif.: Pacific Earthquake Engineering Research (PEER) Center, Univ. of California; 2006.
[28] Fujikake K, Senga T, Ueda N, Ohno T, Katagiri M. Study on impact response of reactive powder concrete beam and its analytical model. J Adv Concr Technol 2006;4:99–108.
[29] Ou Y-C, Nguyen ND. Modified axial-shear-flexure interaction approaches for uncorroded and corroded reinforced concrete beams. Eng Struct 2016;128:44–54.
[30] Karsan ID, Jirsa JO. Behavior of concrete under compressive loadings. J Struct Div 1969;95:2543–63.
[31] Popovics S. A numerical approach to the complete stress-strain curve of concrete. Cem Concr Res 1973;3:583–99.
[32] Guo W, Fan W, Shao XD, Shen DJ, Chen BS. Constitutive model of ultra-high-performance fiber-reinforced concrete for low-velocity impact simulations. Compos Struct 2018;185:307–26.
[33] Japan Society of Civil Engineers (JSCE). Impact behavior and design of structures. Structural Engineering Series 6. Tokyo (in Japanese): JSCE; 1993.
[34] Carta G, Stochino F. Theoretical models to predict the flexural failure of reinforced concrete beams under blast loads. Eng Struct 2013;49:306–15.
[35] Yoo D-Y, Banthia N, Kim S-W, Yoon Y-S. Response of ultra-high-performance fiber-reinforced concrete beams with continuous steel reinforcement subjected to low-velocity impact loading. Compos Struct 2015;126:233–45.
[36] Fan W, Shen D, Yang T, Shao X. Experimental and numerical study on low-velocity lateral impact behaviors of RC, UHPFRC and UHPFRC-strengthened columns. Eng Struct 2019;191:509–25.
[37] Elwood KJ. Modelling failures in existing reinforced concrete columns. Can J Civ Eng 2004;31:846–59.
[38] Ghannoum Wassim M, Moehle Jack P. Rotation-based shear failure model for lightly confined RC columns. J Struct Eng 2012;138:1267–78.
[39] Lee H, Mosalam KM. Seismic evaluation of the shear behavior in reinforced concrete bridge columns including effect of vertical accelerations. Earthq Eng Struct Dyn 2014;43:317–37.
[40] Yi W-J, Zhao D-B, Kunnath SK. Simplified approach for assessing shear resistance of reinforced concrete beams under impact loads. ACI Struct J 2016;113:747–56.
[41] Bentz EC, Vecchio FJ, Collins MR. Simplified modified compression field theory for calculating shear strength of reinforced concrete elements. ACI Struct J 2006;103:614–24.
[42] Adhikary SD, Li B, Fujikake K. Strength and behavior in shear of reinforced concrete deep beams under dynamic loading conditions. Nucl Eng Des 2013;259:14–28.
[43] Vecchio FJ, Collins MP. The modified compression-field theory for reinforced-concrete elements subjected to shear. J Am Concr Inst 1986;83:219–31.
[44] Vecchio FJ. Disturbed stress field model for reinforced concrete: formulation. J Struct Eng-ASCE 2000;126:1070–7.
[45] Zhao D. Response characteristics and design method of reinforced concrete beams under impacting load. Changsha, China: College of Civil Engineering, Hunan University; 2017.
[46] Ferche AC, Panesar DK, Sheikh SA, Vecchio FJ. Toward macro-modeling of alkali-silica reaction-affected structures. ACI Struct J 2017;114:1121–9.
[47] Gu X, Jin X, Zhou Y. Basic principles of concrete structures. Berlin, Heidelberg: Springer; 2016.
[48] Ministry of Communications of China. Code for design of highway reinforced concrete and prestressed concrete bridge and culverts (JTG D62–2004). Beijing: China Communications Press; 2004.
[49] ACI Standard. Building Code Requirements for Structural Concrete (ACI 318-14),. American Concrete Institute; 2014.
[50] Bentz EC. Sectional analysis of reinforced concrete members. Toronto: University of Toronto; 2000.
[51] Xu B, Zeng X. Experimental study on the behaviors of reinforced concrete beams under impact loadings. China Civ Eng J 2014;47:41–51.
[52] Krauthammer T, Bazeos N, Holmquist T. Modified SDOF analysis of RC box-type structures. J Struct Eng 1986;112:726–44.
[53] Gurbuz T, Ilki A, Thambiratnam DP, Perera N. Low-elevation impact tests of axially loaded reinforced concrete columns. ACI Struct J 2019;116.